Advanced Functional Materials

ADVANCED FUNCTIONAL MATERIALS
www.afm-journal.de

RESEARCH ARTICLE OPEN ACCESS

Intrinsic Photoactive Star ZnPc–Poly(glutamate) Nanoplatforms for Multimodal Glioblastoma Therapy and Brain-Targeted Delivery

Amina Benaicha-Fernández[1] | Teodora Ranđelović[2,3] | Ana Armiñán[1,4] | Víctor Sebastián[3,5,6,7] | Manuel Fuentes[4,8,9] | Cristián Huck-Iriart[10] | Esther Masiá[1,4,11] | Paula Carrascosa-Marco[1] | Pablo Juanes-Velasco[8,9] | Snežana Đorđević[12] | Clara Bayona[2] | Ignacio Ochoa[2,3] | Maria Medel[1,4] | Inmaculada Conejos-Sánchez[1,4] | María J. Vicent[1,4,11,13]

[1]Polymer Therapeutics Lab, Príncipe Felipe Research Center (CIPF), València, Spain | [2]Tissue Microenvironment (TME) Lab, Institute for Health Research Aragón (IIS Aragón), Aragón Institute of Engineering Research (I3A), University of Zaragoza, Zaragoza, Spain | [3]CIBERBBN, IISCIII, Zaragoza, Spain | [4]CIBERONC, IISCIII, Madrid, Spain | [5]Department of Chemical Engineering and Environmental Technologies, University of Zaragoza, Zaragoza, Spain | [6]Instituto de Nanociencia y Materiales de Aragón (INMA), CSIC-Universidad de Zaragoza, Zaragoza, Spain | [7]Laboratorio de Microscopías Avanzadas, Universidad de Zaragoza, Zaragoza, Spain | [8]Translational and Clinical Research Program, Cancer Research Center (IBMCC, CSIC), Cytometry Service, NUCLEUS, Department of Medicine, Universidad de Salamanca, Salamanca, Spain | [9]Proteomics Platform, Institute of Biomedical Research of Salamanca (IBSAL), Salamanca, Spain | [10]Experiments Division, ALBA Synchrotron Light Source, Barcelona, Spain | [11]Screening Platform, Príncipe Felipe Research Center, València, Spain | [12]Tosoh Bioscience GmbH, Griesheim, Germany | [13]Department of Medicine, University Jaume I, Castellón, Spain

Correspondence: Maria Medel (mmedel@cipf.es) | Inmaculada Conejos-Sánchez (iconejos@curapath.es) | María J. Vicent (mjvicent@cipf.es)

Received: 2 May 2026 | **Accepted:** 4 May 2026

Keywords: glioblastoma multiforme | multimodal | photoactive polymers | polypeptide–drug conjugate | star-shaped polypeptides | supramolecular assembly | zinc phthalocyanine

ABSTRACT

The design of polymeric systems with intrinsically integrated imaging and responsive functionalities represents a promising strategy to address the complexity of aggressive tumors such as glioblastoma multiforme (GBM). We report a class of star-shaped zinc phthalocyanine–poly(L-glutamic acid) (ZnPc-PGA) nanocarriers in which the photoactive ZnPc core serves as a macroinitiator for the N-carboxyanhydride ring-opening polymerization, enabling control over chain length, architecture, and stoichiometry. ZnPc-PGA nanocarriers exhibited near-infrared absorption, enabling their implementation as imaging agents and photosensitizers for photodynamic therapy. Physicochemical characterization of ZnPc-PGA nanocarriers revealed chain-length- and concentration-dependent supramolecular assembly. ZnPc-PGA nanocarriers demonstrated lysosomal uptake/light-activated cytotoxicity in GBM cells, while evaluation in the GBM-on-a-chip platform confirmed oxygen-dependent therapeutic outcomes. Proteomic profiling revealed a fibrinogen-, cytoskeletal-, and olfactory protein-enriched corona, providing insight into potential biointerface interactions. Post-polymerization conjugation of ZnPc-PGA nanocarriers with paclitaxel facilitated multimodal therapy with enhanced efficacy in GBM cells, while integrating ZnPc-PGA nanocarriers into a hyaluronic acid-based hydrogel enabled intranasal delivery and resulted in brain accumulation. Overall, ZnPc-PGA represents a modular nanoplatform and underscores the role of polymer architecture in dictating behavior in complex biological environments, with potential applicability in the design of multifunctional systems for challenging diseases such as GBM.

---

1 | Introduction

Developing novel therapeutic approaches for hard-to-treat tumors such as glioblastoma multiforme (GBM), characterized by rapid proliferation, diffuse infiltration, and inter-/intra-tumoral heterogeneity) [1, 2], remains a significant challenge. The failure of many therapies stems from the complex biological and anatomical features of GBM, including an immunosuppressive/hypoxic tumor microenvironment (TME), a dense extracellular matrix (ECM) that hinders drug penetration, and infiltrative GBM cells that escape resection margins and colonize healthy parenchyma [3]. The blood–brain barrier (BBB) also restricts the delivery of therapeutic agents, thereby limiting their impact following systemic administration [4]. The development of nanomedicines that cross the BBB and specifically target tumor tissues has therefore garnered interest [5–10]; as such, polymer therapeutics combine non-invasive disease monitoring and chemotherapeutic drug delivery to the brain with phototherapies, immunotherapies, or gene therapy to create nanomedicine-based theranostic platforms [11].

Photodynamic therapy (PDT) combined with fluorescence-guided surgery and real-time imaging provides a non-invasive approach to managing infiltrative tumors such as GBM [12–14]. Near-infrared (NIR) light provides improved tissue penetration and reduced background interference compared to visible light, making associated photosensitizers advantageous for deep-tissue therapy and intraoperative visualization [15]. Unfortunately, first-generation photosensitizers (such as porphyrins) suffer from intrinsic spectral limitations that limit NIR-guided applications [16]. Alternative photosensitizers with improved NIR photophysical properties and more predictable polymer integration (such as phthalocyanines) may offer enhanced versatility for theranostic applications. While structurally related to porphyrins, phthalocyanines possess expanded π-conjugation potential and enhanced photophysical properties, which include strong Q-band absorption, high singlet oxygen quantum yields, robust photostability, and large molar extinction coefficients [17]. Notably, deeper tissue activation and higher reactive oxygen species (ROS) generation make phthalocyanines ideal candidates for the development of PDT-based theranostic platforms. Present phthalocyanine-based hybrid platforms (based on liposome/polymeric micelle formulations, surface conjugation to nanoparticles, or covalent attachment to polymer backbones) [18] exhibit enhanced solubility, tumor accumulation, and therapeutic efficacy in preclinical models; however, they suffer from batch-to-batch heterogeneity and unpredictable in vivo behavior [19, 20].

The intranasal route offers a non-invasive alternative by partially bypassing the BBB through olfactory and trigeminal nerve pathways, enabling direct nose-to-brain transport via extracellular diffusion and neuronal trafficking [21, 22]; nevertheless, mucociliary clearance, enzymatic degradation, and limited dosing volumes constrain intranasal delivery [23, 24]. Nanomedicines can mitigate these challenges by enhancing mucosal retention, protecting cargo, and promoting controlled brain distribution, thereby improving the translational potential of GBM therapies.

We now report the use of zinc phthalocyanine (ZnPc) as a macroinitiator for N-carboxyanhydride ring-opening polymerization (NCA-ROP) to develop a class of star-shaped PGA nanocarriers with defined architectures, tunable arm lengths, and stoichiometric incorporation of the ZnPc core, conferring PDT and drug-loading capacity for GBM theranostics. Characterization of ZnPc-PGA nanocarriers revealed architecture-dependent aggregation behavior that modulated photophysical properties and biological performance, with fluorescence efficiently recovered upon exposure to biological media. This intrinsic fluorescence enabled real-time monitoring of cellular trafficking in 2D and 3D tumor models, where ZnPc-PGA nanocarriers displayed robust cellular uptake and increased ROS generation upon light irradiation. The application of GBM models mimicking hypoxic tumor regions revealed efficient cell uptake of ZnPc-PGA nanocarriers despite the expected reduction in PDT efficacy. Formulation of ZnPc-PGA nanocarriers within a hybrid hyaluronic acid–PGA vehicle (HA-CP, Yalic) enabled intranasal administration and central nervous system (CNS) accumulation. Overall, integrating a photoactive molecule within the polypeptide backbone establishes a modular platform with intrinsic functionality, offering a versatile alternative to conventional post-polymerization modification strategies.

2 | Results and Discussion

2.1 | Design, Synthesis, and Structural Control of ZnPc-PGA Nanocarriers

2.1.1 | Macroinitiated Synthesis Enables the Generation of ZnPc-PGA Nanocarriers

To develop modular nanocarriers with enhanced control over photophysical and structural properties, we synthesized star-shaped PGA polypeptides using a ZnPc macroinitiator bearing four amino termini (Figure 1A). NCA-ROP enabled direct growth of PGA arms, yielding nanocarriers with degrees of polymerization (DP) of 20 (ZnPc–PGA$_{20}$) and 200 (ZnPc–PGA$_{200}$). We expected ZnPc-PGA$_{20}$ to display maximal fluorescence signal and PDT activity by reducing steric constraints around the core (thereby increasing ZnPc exposure) and envisioned ZnPc–PGA$_{200}$ to display improved colloidal stability and drug-loading capacity due to the additional pendant carboxylic groups.

We initially synthesized ZnPc–PGA$_{20}$ using γ-tert-butyl-protected glutamic acid NCA (Glu(OtBu)-NCA), which enabled controlled chain growth and high monomer conversion in dry dimethyl formamide (DMF); however, this approach proved impractical for ZnPc–PGA$_{200}$ due to extended reaction times, partial monomer degradation, and limited scalability. We transitioned to γ-benzyl-protected glutamic acid NCA (Glu(OBzl)-NCA), a more stable monomer widely used for higher-DP PGA synthesis [25], to improve reproducibility, shorten reaction times, and increase yields. We tailored solvent choice to each monomer: DMF for Glu(OtBu)-NCA, which supported the controlled synthesis of ZnPc–PGA$_{20}$, whereas the higher monomer loading required for ZnPc–PGA$_{200}$ demanded a solvent with greater solubilizing power. We employed dimethyl sulfoxide (DMSO) for Glu(OBzl)-NCA polymerization, ensuring the complete solubilization of the ZnPc macroinitiator and the benzyl-protected NCA, thereby minimizing premature aggregation and facilitating uniform arm growth. In all synthetic approaches, we added the monomer dropwise using a cannula under anhydrous conditions to maintain low

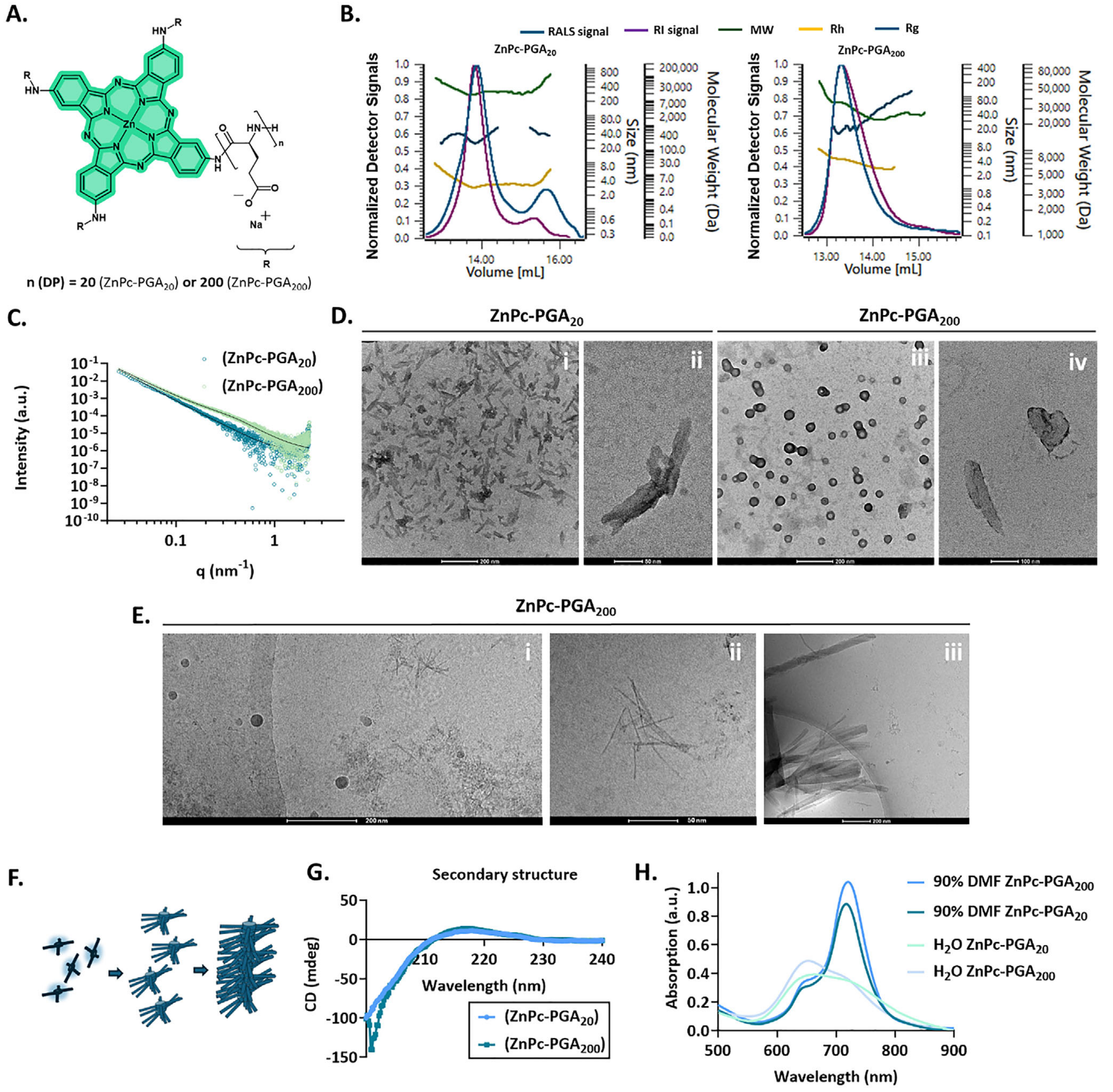

FIGURE 1 | Synthesis and physicochemical characterization of ZnPc-PGA$_{20}$ and ZnPc-PGA$_{200}$. (A) Schematic representation of ZnPc-PGA with a DP of 20 (ZnPc-PGA$_{20}$) and 200 (ZnPc-PGA$_{200}$). (B) Mw, Rg, and Rh distribution of ZnPc-PGA$_{20}$ and ZnPc-PGA$_{200}$ determined by SEC-RI-MALS-viscometer analysis. (C) SAXS intensity as a function of the scattering momentum transfer, q ($q = 4\pi \sin \theta / \lambda$). (D) TEM images depicting ZnPc-PGA$_{20}$ forming cylindrical structures at (i) 2 mg mL^{-1} (scale bar = 200 nm) and (ii) 0.25 mg mL^{-1} (scale bar = 50 nm) and ZnPc-PGA$_{200}$ forming (iii) spherical architectures at 2 mg mL^{-1} (scale bar = 200 nm) and (iv) cylindrical assemblies at 0.25 mg mL^{-1} (scale bar = 100 nm). (E) Cryo-TEM images depicting ZnPc-PGA$_{200}$ forming (i) spherical architectures (scale bar = 200 nm) and (ii) cylindrical architectures (scale bar = 50 nm) at 2 mg mL^{-1} and (III) cylindrical assemblies at 0.25 mg mL^{-1} (scale bar = 200 nm). (F) Illustration of spontaneous self-assembly of ZnPc-PGA nanocarriers into supramolecular nanostructures in aqueous media. (G) CD spectra of ZnPc-PGA$_{20}$ and ZnPc-PGA$_{200}$ in PBS. (H) UV–vis absorbance spectra of ZnPc-PGA$_{20}$ at 0.2 mg mL^{-1} (H_2O) and 0.05 mg ml^{-1} (DMF) and ZnPc-PGA$_{200}$ at 0.6 mg mL^{-1} (H_2O and DMF).

local concentration, prevent uncontrolled homopolymerization, and preserve the star-shaped architecture (Scheme S1), which ensured simultaneous arm growth and low batch-to-batch dispersity. After polymerization, we fully deprotected the benzyl and tert-butyl groups using trifluoroacetic acid (TFA)/hydrogen bromide (HBr) at room temperature, which we confirmed via ^{1}H-NMR analysis (Figure S1 – ZnPc–PGAOtBu$_{20}$; Figure S2 – ZnPc–PGAOBzl$_{200}$). Neutralization with 0.05 M aqueous bicarbonate yielded water-soluble ZnPc-PGA sodium salts; we purified the products by dialysis against deionized water and lyophilized them to obtain ZnPc–PGA$_{20}$ and ZnPc–PGA$_{200}$ as green powders (Figures S3 and S4).

TABLE 1 | Physicochemical properties of ZnPc-PGA nanocarriers.

Compound	MW (kDa)[a]	Đ[a]	Rg (nm) by MALS[a]	Rg (nm) by SAXS[b]	Rh (nm) by RI-Viscometer[c]	Rh (nm) by DLS[d]	PDI[d]	Zeta Potential (mV)[d]
ZnPc-PGA$_{20}$	24.5	1.08	36.3	N/D	3.5	18 ± 5	0.343 ± 0.028	−28.5 ± 1.6
ZnPc-PGA$_{200}$	27.0	1.01	38.0	7.8±0.8	4.0	19 ± 4	0.361 ± 0.017	−29.7 ± 1.5

Abbreviations: Mw – molecular weight; Đ – polydispersity; Rg – radius of gyration; Rh – radius of hydration; PDI – polydispersity index for Rh by DLS; N/D – not determined by SAXS.

[a] Determined by SEC-RI-MALS at 4.65 mg mL^{-1};

[b] Determined by SAXS at 0.25 mg mL^{-1};

[c] Determined by SEC-RI-Viscometer at 4.65 mg mL^{-1};

[d] Determined by DLS at 0.25 mg mL^{-1}.

2.1.2 | Molecular Characterization Confirms Defined Size and Stoichiometry of ZnPc-PGA Nanocarriers

Comprehensive physicochemical analyses by size exclusion chromatography using refractive index and multi-angle light scattering (SEC-RI-MALS)-viscometry, ^{1}H-NMR, dynamic light scattering (DLS), small-angle X-ray scattering (SAXS), and ultraviolet–visible (UV–vis) spectroscopy confirmed narrow polydispersity (Đ < 1.1), accurate ZnPc:PGA stoichiometry, reproducible molecular weight (Mw), and distinct aggregation behaviors (Table 1, Figure 1; Table S2 and Figure S5). Importantly, SEC-RI-MALS analysis confirmed batch-to-batch reproducibility of ZnPc-PGA$_{200}$, demonstrating the reliability of the optimized synthetic route for future scale-up and translational efforts (Table S2). SEC-RI-MALS analysis also determined radius of gyration (Rg) values of 36.3 nm for ZnPc-PGA$_{20}$ and 38 nm for ZnPc-PGA$_{200}$, indicating aggregation of both nanocarriers in aqueous media (at ∼4 mg ml^{-1}) (Figure 1B and Table 1). These findings also helped to explain the slight differences in Mw observed in aqueous media between ZnPc–PGA$_{20}$ (24.5 kDa) and ZnPc–PGA$_{200}$ (27.0 kDa), despite the intended ∼ten-fold difference in chain length. The star-shaped architecture and strong π–π stacking interactions of the ZnPc cores promote supramolecular aggregation, altering elution behavior in SEC, thereby compressing the apparent differences in Mw. These observations underscored the need to corroborate findings with orthogonal techniques (e.g., DLS or SAXS).

The size values obtained from different characterization techniques reflected the distinct physical properties of each methodology and highlighted the concentration- and environment-dependent behavior of ZnPc-PGA nanocarrier assemblies. SEC-based analyses revealed hydrodynamic radius (Rh) values of 3.5 nm for ZnPc-PGA$_{20}$ and 4–7 nm for ZnPc-PGA$_{200}$ (Table 1), describing the intrinsic hydrodynamic size of individual polypeptide chains in dilute, non-aggregating organic solvents. Notably, the Rg/Rh ratio determined by SEC-RI-MALS-viscometer analysis for ZnPc–PGA$_{200}$ lies between 1.9 and 2.0, indicative of elongated or cylindrical morphologies (Table 1); this ratio serves as a valuable shape descriptor, with values > 1.5 typically suggesting rod-like or anisotropic assemblies. In contrast, DLS measurements in aqueous media yielded larger Rh values for ZnPc–PGA$_{20}$ (∼18 nm) and ZnPc–PGA$_{200}$ (∼19 nm) (Table 1), which reflects the presence of solvated supramolecular assemblies and small populations of larger aggregates that skew intensity-weighted averages. Consistent with the polyanionic nature of PGA, both ZnPc-PGA$_{20}$ and ZnPc-PGA$_{200}$ exhibited markedly negative ζ-potentials in aqueous media (∼-29 mV), reflecting the deprotonated γ-carboxylate groups along the PGA backbone (Table 1). SAXS determined an Rg value of 7.8 nm for ZnPc-PGA$_{200}$ but failed to reliably analyze ZnPc-PGA$_{20}$, as the shorter PGA chains promoted the formation of large aggregates that fell outside the measurable q-range and prevented accurate Guinier fitting (Figure 1C and Table 1). The discrepancies in Rg values between SEC-RI-MALS and SAXS may be due to differences in the concentrations used in the experiments. The SAXS result indicates that higher concentrations of ZnPc-PGA$_{200}$ lead to aggregation, consistent with the SEC-RI-MALS results (Rg of 38 nm at 4 mg mL^{-1}).

Examining assembly by SAXS revealed that ZnPc-PGA$_{20}$ and ZnPc-PGA$_{200}$ displayed distinct supramolecular behavior in aqueous media; in most cases, the SAXS patterns remained consistent with those of elongated particles described using cylindrical symmetry (a behavior likely driven by the planar nature of the molecular core), which favors π–π interactions and the stacking of multiple units into one-dimensional elongated assemblies (Figure 1C). Quantitative analysis using the Guinier–Porod model yielded a Rg value of ∼7.8 nm for ZnPc-PGA$_{200}$ in a highly diluted solution (0.25 mg mL^{-1}). At 0.5 mg mL^{-1}, nearly all ZnPc-PGA$_{200}$ samples displayed extensive aggregation, with only partial redissolution observed upon further concentration increase (Figures S6–S8 and Table S3 for concentrations 0.25 to 2 mg mL^{-1} of ZnPc-PGA$_{200}$). Nonetheless, we observed a larger particle size than in the most diluted samples for ZnPc-PGA$_{200}$ at 2 mg mL^{-1}, indicating that higher concentrations favor the growth of supramolecular assemblies rather than complete disaggregation. As noted above, we were unable to analyze ZnPc-PGA$_{20}$ by SAXS.

Transmission electron microscopy (TEM) images confirmed distinct supramolecular morphologies for ZnPc–PGA$_{20}$ and ZnPc–PGA$_{200}$. ZnPc–PGA$_{20}$ consistently formed rigid cylindrical aggregates at high and low concentrations (Figure 1D; i: 2 mg mL^{-1} and ii: 0.25 mg mL^{-1}), reflecting the structural rigidity and strong π–π stacking interactions associated with the shorter PGA chains. In contrast, ZnPc–PGA$_{200}$ formed spherical assemblies at higher concentrations (Figure 1D; iii: 2 mg mL^{-1}), while cylindrical features re-emerged at lower concentrations (Figure S9; 1 mg mL^{-1} and Figure 1D; iv: 0.25 mg mL^{-1}). This concentration-dependent morphological variability may stem from the partial collapse of the more hydrated, less structurally stable longer chains during solvent evaporation for

TEM sample preparation. Consistent with the TEM observations, scanning electron microscopy images displayed elongated cylindrical assemblies alongside collapsed regions that appeared as compact clusters of mini-cylindrical substructures, likely reflecting partial deformation during lyophilization (Figures S10 and S11). To clarify whether the spherical structures observed for ZnPc–PGA$_{200}$ at 2 mg mL^{-1} represented true coexisting morphologies, we performed complementary cryo-TEM analysis, which preserves native supramolecular organization. Cryo-TEM revealed the same concentration-dependent behavior observed in conventional TEM: at higher concentrations, ZnPc–PGA$_{200}$ displayed a mixture of spherical assemblies (Figure 1E; i: 2 mg mL^{-1}) and shorter cylindrical segments (Figure 1E; ii: 2 mg mL^{-1}), whereas at lower concentrations, elongated cylindrical aggregates constituted the dominant species, often forming larger supramolecular constructs (Figure 1E; iii: 0.25 mg mL^{-1}). These findings demonstrate that spherical morphologies do not represent preparation artifacts but reflect accurate concentration-dependent assembly, in which longer PGA chains impart a more dynamic aggregation profile: polymer-driven packing dominates at higher concentrations (yielding spheres and short cylinders), while at lower concentrations, ZnPc–ZnPc interactions prevail, stabilizing predominantly cylindrical architectures. Figure 1F illustrates the proposed self-assembly pathways, emphasizing chain-length-dependent aggregation behavior. Complementary circular dichroism (CD) spectroscopy confirmed that ZnPc–PGA$_{20}$ and ZnPc–PGA$_{200}$ retained random-coil conformations in aqueous media (Figure 1G), indicating that PGA arms remain unstructured despite ZnPc-driven aggregation.

UV–vis spectroscopy-based analysis revealed that ZnPc–PGA$_{20}$ and ZnPc–PGA$_{200}$ displayed obvious signs of aggregation in aqueous media, including broadened and redshifted Q-bands (715 nm) characteristic of π–π stacking among ZnPc cores (Figure 1H). We also found evidence for the stronger aggregation of ZnPc–PGA$_{20}$ in aqueous media via a pronounced increase in the Q-band at 715 nm upon addition of DMF, a solvent-induced disaggregation effect that required dilution of the sample from 0.20 to 0.05 mg mL^{-1} for the baseline spectra to fall within the linear range (ZnPc–PGA$_{200}$ did not require dilution). This aggregation behavior remained consistent across differing media conditions, including altered ionic strength (phosphate-buffered saline; PBS), mildly acidic pH (5.5), and dilution, indicating high structural stability. DLS confirmed that hydrodynamic sizes (Figure S12) and fluorescence signals (Figure S13) did not change significantly upon dilution, suggesting that the self-assembled aggregates persist under physiological-like conditions.

ZnPc–PGA$_{20}$ and ZnPc–PGA$_{200}$ exhibited similar optical responses despite differences in chain length, highlighting the dominant influence of ZnPc–ZnPc interactions on their photophysical behavior (Figure 1H).

The strong stacking interactions led to fluorescence quenching, potentially compromising performance in imaging or PDT (Figure S13). While aggregation can reduce photobleaching by dissipating excitation energy, excessive stacking can limit fluorescence emission and overall photophysical output [26]; thus, fluorescence recovery under physiological-like conditions remains essential for functional deployment. To demonstrate fluorescence recovery in biologically relevant conditions, we incubated ZnPc–PGA$_{20}$ and ZnPc–PGA$_{200}$ in 10% fetal bovine serum (FBS) in PBS; in both cases, fluorescence emission increased compared to PBS buffer alone (Figure S13), suggesting that protein–polypeptide interactions partially disrupted π–π stacking or altered the local microenvironment. This result aligns with the known ability of serum proteins to interact with hydrophobic or aromatic domains [27, 28], thereby modulating supramolecular packing.

In summary, comprehensive physicochemical characterization integrating SEC-RI-MALS-viscometry, ^{1}H-NMR, DLS, SAXS, UV–vis spectroscopy, and TEM collectively described the structural identity, batch-to-batch reproducibility, and robust supramolecular behavior of ZnPc-PGA nanocarriers. Despite their intended differences in chain length, ZnPc–PGA$_{20}$ and ZnPc–PGA$_{200}$ exhibited pronounced π–π-driven aggregation in aqueous media, compressing their apparent Mw differences and generating concentration-dependent elongated assemblies with Rg/Rh ratios ~2, consistent with a cylindrical morphology. Orthogonal analyses confirmed formation of stable supramolecular aggregates in aqueous media, with SAXS and TEM demonstrating chain-length- and concentration-dependent assembly behavior. UV–vis and fluorescence studies further supported strong ZnPc–ZnPc interactions, while partial fluorescence recovery in serum-containing media suggested biologically relevant modulation of aggregation.

2.1.3 | Analysis of ZnPc-PGA Nanocarrier Protein Corona Suggests Potential Biointerface Interactions

Upon entering biological fluids, nanocarriers encounter a complex, protein-rich environment that drives spontaneous protein adsorption, leading to the formation of a protein corona [29, 30]. This phenomenon reshapes the physicochemical identities of nanocarriers and influences colloidal stability, cellular recognition, biodistribution, and therapeutic performance [31] and also modulates processes such as drug release, cellular uptake, and immune interactions [32]. We characterized ZnPc-PGA nanocarrier-associated coronae by incubating ZnPc–PGA$_{20}$ and ZnPc–PGA$_{200}$ with human serum. Following established protocols, we distinguished hard and soft corona layers, isolated nanocarrier–protein complexes, and processed associated proteins using a standardized in-StageTip workflow for complete lysis, digestion, and peptide cleanup prior to liquid chromatography-tandem mass spectrometry (LC-MS/MS) analysis.

We acquired and processed MS data using a data-independent acquisition method and integrated software to generate label-free quantitative protein profiles for ZnPc–PGA$_{20}$ and ZnPc–PGA$_{200}$. From the complete proteomic dataset, we selected the 20 most abundant proteins for comparative analysis (the Supporting Information provides complete lists of associated cellular components, molecular functions, and biological processes). Annotation of protein identities for ZnPc–PGA$_{20}$ (Figure 2A) and ZnPc–PGA$_{200}$ (Figure 2B) via the UniProt database revealed consistent protein profiles. Functional Reactome pathway analysis (Figure 2C,D) indicated enrichment in biological pathways including coagulation cascades, cell–cell adhesion, intracellular

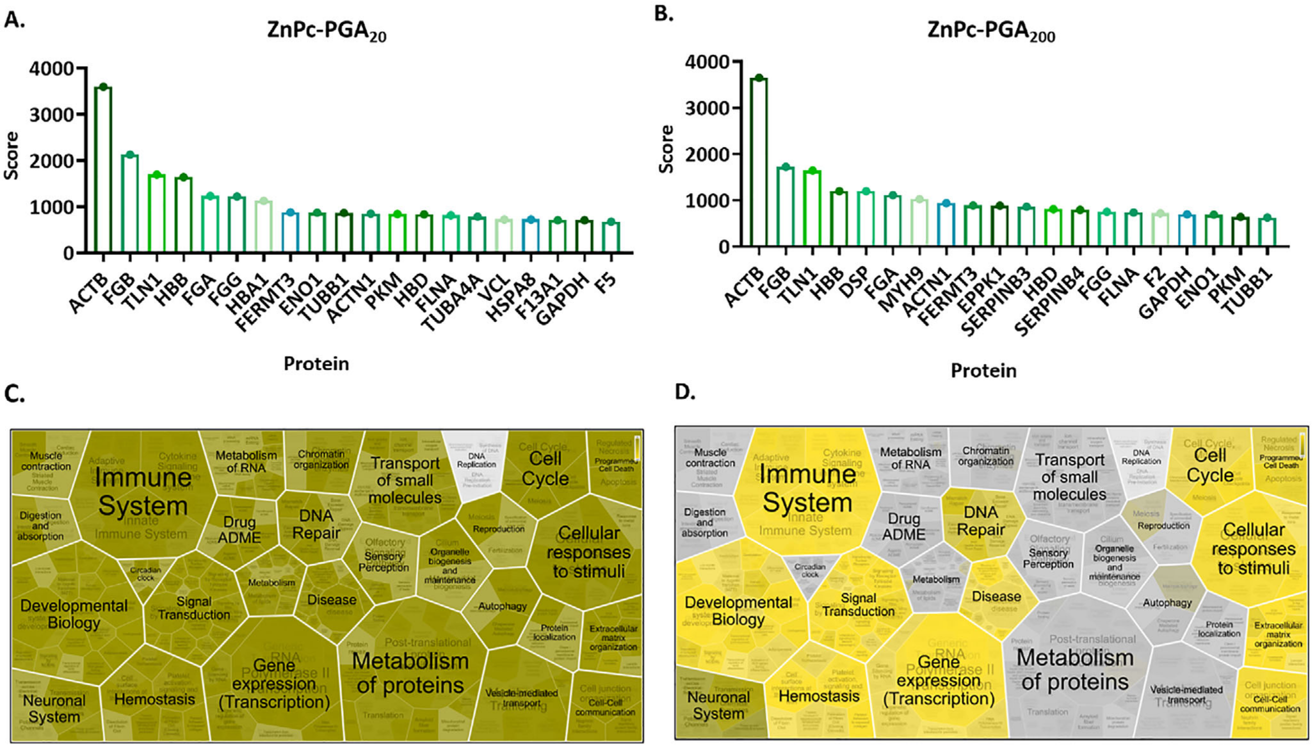

FIGURE 2 | Analysis of ZnPc-PGA$_{20}$ and ZnPc-PGA$_{200}$ protein coronae: Abundant proteins and functional enrichment. (A,B) Top 20 most abundant proteins of the (A) ZnPc-PGA$_{20}$ and (B) ZnPc-PGA$_{200}$ protein coronae. (C,D): Reactfoam graphs generated via Reactome (www.reactome.org) illustrate functional pathway enrichment among the 20 most abundant corona proteins from (C) ZnPc-PGA$_{20}$ and (D) ZnPc-PGA$_{200}$. Tile color intensity (yellow > gray) and size reflect relative enrichment and representation of pathway categories, respectively. Shared features include immune system activity, protein metabolism, and olfactory signaling. ACTB (Actin, cytoplasmic 1), ACTN1 (Isoform 2 of Alpha-actinin-1), DSP (Desmoplakin), ENO1 (Alpha-enolase), EPPK1 (Epiplakin), F13A1 (Coagulation factor XIII A chain), F2 (Prothrombin), F5 (Coagulation factor V), FERMT3 (Isoform 2 of Fermitin family homolog 3), FGA (Isoform 2 of Fibrinogen alpha chain), FGB (Fibrinogen beta chain), FGG (Isoform Gamma-A of Fibrinogen gamma chain), FLNA (Isoform 2 of Filamin-A), GAPDH (Glyceraldehyde-3-phosphate dehydrogenase), HBA1 (Hemoglobin subunit alpha), HBB (Hemoglobin subunit beta), HBD (Hemoglobin subunit delta), HSPA8 (Heat shock cognate 71 kDa protein), MYH9 (Myosin-9), PKM (Pyruvate kinase PKM), SERPINB3 (Serpin B3), SERPINB4 (Serpin B4), TLN1 (Talin-1), TUBA4A (Isoform 2 of Tubulin alpha-4A chain), and TUBB1 (Tubulin beta-1 chain), and VCL (Vinculin).

trafficking, cytoskeletal regulation, olfactory signaling, innate immunity, and ECM remodeling.

A quantitative comparison of coronal composition revealed a high degree of similarity between ZnPc–PGA$_{20}$ and ZnPc–PGA$_{200}$ despite their distinct chain lengths and ZnPc:PGA ratios (Figure 2A,B). Dominant protein classes consistently recruited by ZnPc–PGA$_{20}$ and ZnPc–PGA$_{200}$ included proteins that frequently occur in the hard coronas of blood-exposed nanomaterials, [29, 30], such as cytoskeletal proteins (ACTB, ACTN1, FLNA, TLN1, and VCL), fibrinogen chains (FGA, FGB, and FGG), hemoglobin subunits (HBB, HBA1, and HBD), and metabolic enzymes (GAPDH, ENO1, aPKM).

Functional annotation revealed enrichment in biological pathways related to macrocomplexes (commonly found in peripheral blood, including platelet-coagulation proteins and lipoproteins), cell–cell contact (e.g., integrins and cytoskeletal elements), intracellular trafficking, metabolic processes, olfactory signaling, innate immune response, stimulus sensing, and hemostasis (Figure 2C,D). Protein origin tracing via the Human Protein Atlas revealed that most adsorbed proteins originated from plasma, ECM, mucosa, epithelium, or endothelium (tissue sources highly relevant to vascular and nasal exposure routes). Notably, the consistent enrichment of fibrinogen components (FGA, FGB, and FGG) in coronae suggests the potential for interactions with endothelial integrins, which studies have linked to enhanced vascular adhesion, altered biodistribution, and, in some cases, accelerated clearance through the mononuclear phagocyte system [33, 34]. Fibrinogen adsorption also represents a known trigger of complement activation and immune recognition, depending on the conformation and exposure of cryptic domains [35]. Conversely, an abundance of cytoskeletal and adhesion-associated proteins, such as actin isoforms, talin, filamin, and vinculin (commonly referred to as “dysopsonins”), attenuate immune recognition, reduce complement cascade activation, and extend nanoparticle circulation time [36, 37]. These proteins may confer “stealth-like” properties by suppressing phagocytic immune cell uptake, thereby modulating biodistribution in favor of longer systemic residence and targeted tissue accumulation.

Interestingly, Reactome pathway analysis via Reactfoam revealed significant enrichment in proteins associated with olfactory signaling pathways for ZnPc–PGA$_{20}$ and ZnPc–PGA$_{200}$ (Figure 2C,D). In particular, we identified pathway clusters related to G protein-coupled receptor signaling, sensory perception, and olfactory receptor activity within the top-tier enrichment categories, indicating that proteins within the corona participate in molecular recognition processes commonly associated with the nasal epithelium and chemosensory interfaces. These features suggest an unanticipated functional interface between the protein corona and the olfactory mucosa, which may facilitate epithelial adhesion, neural translocation, or even CNS entry, mechanisms particularly relevant to intranasal delivery strategies [38].

Notably, this olfactory signaling signature emerged alongside other consistently enriched pathways, including those related to innate immunity, vesicular trafficking, protein metabolism, hemostasis, and the immune system at large, as visualized in the clustering and coloring patterns of the Reactfoam graphs (Figure 2C,D). The yellow coloration and larger tile areas corresponding to these pathways (Figure 2C,D) indicate higher representation and statistical enrichment among the identified protein datasets for ZnPc–PGA$_{20}$ and ZnPc–PGA$_{200}$. The consistent presence of olfactory-related and mucosa-relevant proteins in the ZnPc–PGA$_{20}$ and ZnPc–PGA$_{200}$ coronae suggests that they may contribute to immune shielding and region-specific mucosal targeting through corona-mediated epithelial interactions. This hypothesis aligns with emerging perspectives in nanomedicine that describe the protein corona as a "protein–nanoparticle alliance" [39], a biologically active layer that can direct tissue tropism and biodistribution, particularly across mucosal and endothelial barriers.

Although ZnPc–PGA$_{20}$ and ZnPc–PGA$_{200}$ differ in chain length and ZnPc content, their aggregation behavior in aqueous media and random-coil conformations likely yield comparable surface presentation, leading to similar corona formation. As such, both systems demonstrate a consistent, biologically relevant protein corona, which may underpin favorable biodistribution and therapeutic performance. Overall, the formation of a fibrinogen-, cytoskeletal-, and olfactory protein-enriched corona suggests that this protein–nanoplatform alliance may support immune evasion, endothelial interaction, and enhanced CNS delivery via intranasal routes. Nevertheless, further targeted in vitro and in vivo studies will be required to experimentally elucidate the precise role of these corona-associated proteins in mediating nanoplatform transport, cellular interactions, and biological responses.

2.2 | ZnPc-PGA$_{20}$ and ZnPc-PGA$_{200}$ Exhibit Efficient Cellular Uptake and Light-Activated Cytotoxicity in GBM Cells

The intrinsic fluorescence of the ZnPc core enables real-time tracking of cellular uptake and intracellular trafficking without the need for additional dyes. We quantified uptake kinetics using flow cytometry in A172 and U251MG GBM cells at 37°C (Figure 3A) and 4°C (Figure S14) to differentiate energy-dependent internalization mechanisms (e.g., endocytosis) from passive uptake (e.g., diffusion). At 37°C, ZnPc-PGA$_{20}$ and ZnPc-PGA$_{200}$ exhibited time-dependent increases in fluorescence intensity (FI), reaching a plateau around 48 h and remaining sustained through 72 h, indicating stable intracellular retention (Figure 3A). In contrast, uptake at 4°C remained minimal and unchanged across time points (Figure S14), confirming that cellular internalization of ZnPc–PGA$_{20}$ and ZnPc–PGA$_{200}$ proceeds primarily via an energy-dependent endocytic pathway. Surprisingly, ZnPc–PGA$_{200}$ exhibited significantly higher intracellular fluorescence at 24 and 48 h compared to ZnPc–PGA$_{20}$ for both cell lines ($^*p \leq 0.05$); however, this apparent difference disappeared at 72 h, when ZnPc–PGA$_{20}$ and ZnPc–PGA$_{200}$ reached comparable fluorescence intensities. Rather than reflecting greater internalization of ZnPc–PGA$_{200}$, we attributed these transient differences to differences in aggregation state between the distinct architectures. The shorter ZnPc–PGA$_{20}$ exhibits greater structural stability and slower intracellular disaggregation, resulting in delayed fluorescence recovery compared to ZnPc–PGA$_{200}$; consequently, the early-time differences in fluorescence reflect photophysical unquenching kinetics rather than real disparities in cellular uptake. Despite differences in nanocarrier PGA arm length, ZnPc–PGA$_{20}$ and ZnPc–PGA$_{200}$ displayed similar uptake kinetics at equimolar ZnPc concentrations, suggesting that PGA length does not significantly alter uptake efficiency under these conditions; moreover, nearly all cells displayed detectable fluorescence within 30 min of incubation (Figure S15), indicating rapid membrane association and early endocytic engagement.

Given the known tropism of ZnPc (and derivatives) for mitochondria and/or lysosomes (organelles that critically influence the photodynamic response) [40], we employed fluorescence confocal microscopy to investigate the intracellular trafficking and subcellular localization of ZnPc-PGA nanocarriers. Live-cell confocal fluorescence microscopy at 24 h post-incubation in A172 and U251MG cells revealed punctate red fluorescence patterns for ZnPc–PGA$_{20}$ and ZnPc–PGA$_{200}$, consistent with vesicular localization following endocytic internalization (Figure 3B). We excluded earlier time points from imaging due to insufficient signal, consistent with the flow cytometry-quantified uptake kinetics. Co-staining with LysoTracker Blue and Mitotracker Green confirmed partial colocalization of ZnPc fluorescence with lysosomal compartments, as evidenced by purple puncta in merged images, suggesting endo-lysosomal sequestration. These findings support a common intracellular trafficking pathway for ZnPc-based macromolecules, in which uptake occurs via energy-dependent endocytosis, followed by retention within acidic vesicles [40, 41]. The lysosomal compartmentalization of ZnPc–PGA$_{20}$ and ZnPc–PGA$_{200}$ holds important mechanistic implications; lysosomes function as stable intracellular depots for phthalocyanine-based photosensitizers, whose planar macrocyclic structures exhibit high coordination stability and photostability [40, 41]. This localization promotes localized ROS generation upon NIR irradiation while potentially minimizing off-target cytotoxicity, thus enhancing therapeutic precision. Notably, ZnPc–PGA$_{20}$ and ZnPc–PGA$_{200}$ displayed comparable subcellular localization and FI when administered at equimolar ZnPc concentrations, indicating that variations in PGA chain length do not significantly affect internalization behavior or monitoring capabilities. The persistence of the ZnPc signal after 24 h further suggests stable intracellular retention of the ZnPc core, due to its high coordination stability and propensity for lysosomal accumulation, whereas the PGA arms may undergo intracellular degradation [25]. Together, these results demonstrate that ZnPc–PGA$_{20}$ and ZnPc–PGA$_{200}$ engage endo-lysosomal pathways and enable sustained intracellular fluorescence, a requirement for subsequent photoactivation and therapeutic function.

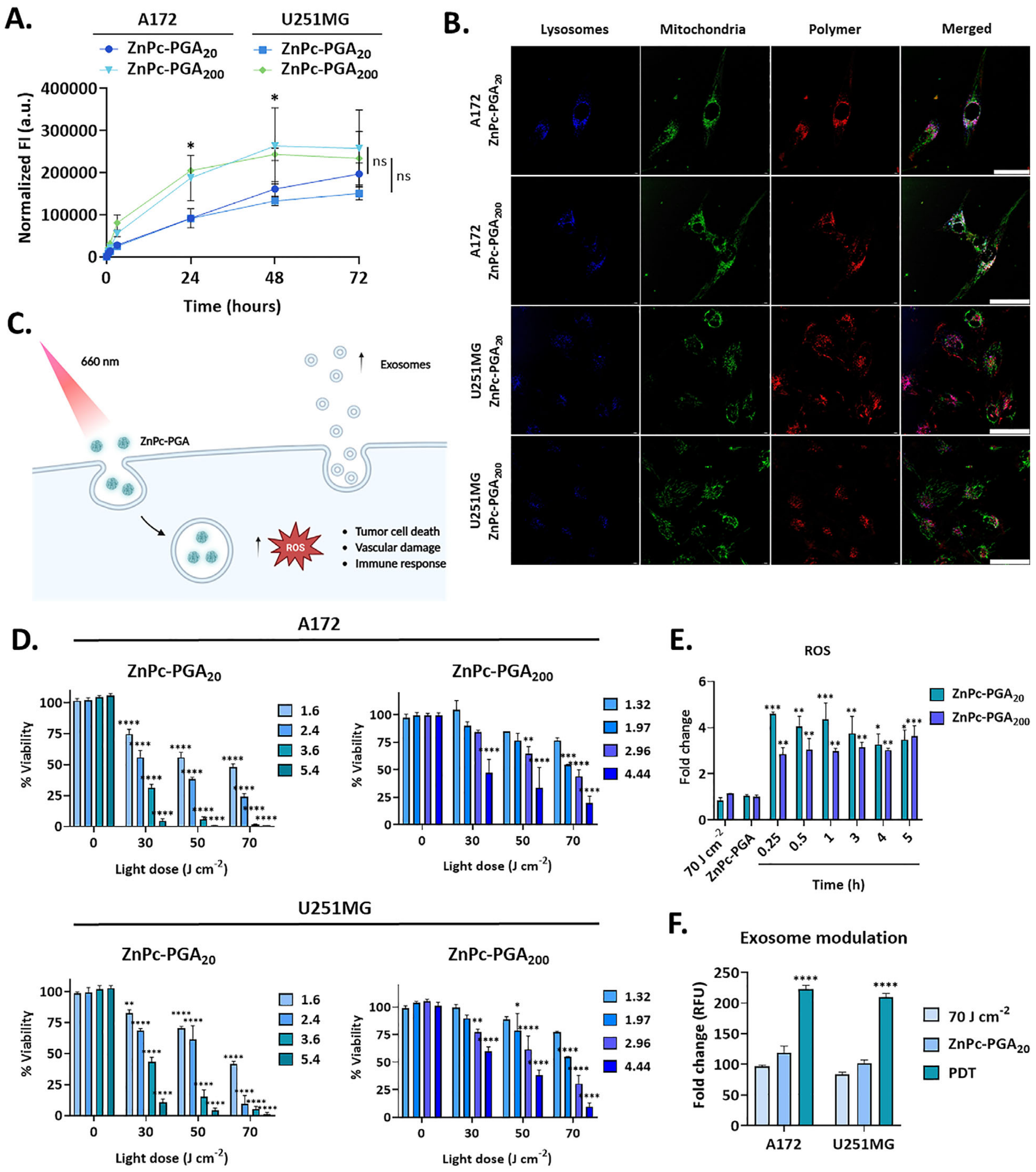

FIGURE 3 | Cellular uptake and PDT activity of ZnPc-PGA$_{20}$ and ZnPc-PGA$_{200}$. (A) ZnPc-PGA$_{20}$ and ZnPc-PGA$_{200}$ uptake kinetics were quantified by flow cytometry at 0.5, 1, 3, 24, 48, and 72 h in A172 and U251MG cells at 37°C. Two-way ANOVA test compared normalized fluorescence intensity (FI) in arbitrary units (a.u.) between ZnPc-PGA$_{20}$ and ZnPc-PGA$_{200}$ for each time point; $n = 3$, mean ± SEM. Significance reported as $*p \leq 0.05$, ns = non-significant. (B) Confocal microscopy images of ZnPc-PGA$_{20}$ and ZnPc-PGA$_{200}$ intracellular localization in A172 and U251MG cells at 24 h post-treatment (Blue – LysoTracker Blue for lysosomes; Green – MitoTracker Green for mitochondria; Red – ZnPc-PGA fluorescence.) Scale bars = 100 µm. (C) Schematic illustration of the PDT mechanism mediated by ZnPc-PGA, depicting ROS generation and exosome release following irradiation. *Created with BioRender.com*. (D) A172 and U251MG cell viability was measured by MTS assay, measuring PDT activity after incubation with ZnPc-PGA$_{20}$ and ZnPc-PGA$_{200}$ at increasing concentrations and irradiated at 660 nm with different light doses. A two-way ANOVA test compared each ZnPc-PGA PDT dose to respective non-irradiated controls; $n = 3$, mean ± SEM. Significance reported as $*p \leq 0.05$, $**p \leq 0.01$, $***p \leq 0.001$, $****p \leq 0.0001$. (E) Analysis of ROS generation determined by DCFH assay in A172 cells. Data expressed as fold change in relative fluorescence units (RFU) to respective untreated controls; one-way ANOVA test compared each time point to respective irradiated controls, and only-irradiated (70 J cm^{-2}) or only-incubated (ZnPc-PGA) to respective non-treated controls; $n = 3$, mean ± SEM. Significance reported as $*p \leq 0.05$, $**p \leq 0.01$, $***p \leq 0.001$. (F). Modulation of exosome abundance in A172 and U251MG cells assessed by AlphaScreen technology. Data expressed as fold change inRFUs to untreated control; two-way ANOVA test comparing each condition to control (set as 100%); $n = 3$, mean ± SEM. Significance reported as $****p \leq 0.0001$.

We next assessed PDT-mediated cytotoxicity of ZnPc–PGA$_{20}$ and ZnPc–PGA$_{200}$ in A172 and U251MG cells to evaluate therapeutic efficacy (Figure 3C); we incubated cells with increasing concentrations of ZnPc equivalents (from 1.32 to 5.2 μM; corresponding to 1.02–21.15 μg mL^{-1} for ZnPc–PGA$_{20}$ and 34.34–116 μg mL^{-1} for ZnPc–PGA$_{200}$) for 48 h (maximum FI), and then irradiated cells at 660 nm with escalating light doses (0, 30, 50, and 70 J cm^{-2}) (Figure 3D). At the highest light intensity and nanocarrier dose, ZnPc–PGA$_{20}$ and ZnPc–PGA$_{200}$ induced widespread, almost complete cell death; however, PGA or irradiation alone failed to induce cytotoxicity (Figure 3D). Dose-response analyses at 70 J cm^{-2} revealed a lack of statistically significant IC$_{50}$ values between cell lines; however, A172 cells displayed higher sensitivity to ZnPc–PGA$_{20}$ than to ZnPc–PGA$_{200}$ ($^*p \leq 0.05$, Table S4), reinforcing the functional relevance of nanocarrier architecture.

We performed mechanistic studies of PDT-induced cell death using ZnPc-PGA$_{20}$, which exhibited enhanced PDT performance and greater fluorescence sensitivity, making this nanocarrier a suitable candidate for dissecting intracellular pathways of cytotoxicity. To explore the mechanism of PDT, we quantified intracellular ROS generation using the 2′,7′-dichlorodihydrofluorescein (DCFH) assay in A172 cells using ZnPc–PGA$_{20}$ and ZnPc–PGA$_{20}$ (of note, we could not quantify ROS levels in U251MG cells due to cell aggregation artifacts during extended incubation) (Figure 3E). Treatment with ZnPc-PGA$_{20}$ or irradiation alone failed to induce ROS production; however, ZnPc-PGA$_{20}$ treatment followed by irradiation led to a rapid and sustained significant increase in ROS levels, detectable from 0.25 to 5.0 h post-irradiation, consistent with type-II photoreactions mediated by ZnPc in its excited state [40].

PDT stimulates the release of extracellular vesicles, including exosomes, from tumor cells [42], which contribute to immune activation and the proliferation/migration of tumor cells [43–45]. To assess whether ZnPc-PGA-supported PDT-induced extracellular vesicle release, we employed the ExoScreen assay, a bead-based AlphaScreen platform that employs the antibody-mediated detection of the exosomal tetraspanins CD9 and CD63 [46]. We incubated A172 and U251MG cells for 48 h with sub-IC$_{50}$ concentrations of ZnPc–PGA$_{20}$ and then exposed them to 660 nm light at a dose of 70 J cm^{-2} (Figure 3F). ZnPc–PGA$_{20}$ alone or light irradiation (70 J cm^{-2}) alone did not significantly alter exosome levels compared to untreated controls; however, ZnPc–PGA$_{20}$ treatment combined with irradiation (PDT) led to a significant increase in exosome release from both cell lines (normalized to cell viability) (Figure 3F). This finding suggests that PDT-induced cellular stress, even at non-lethal doses, may enhance intercellular signaling via exosomal pathways; however, the precise immunological consequences remain unelucidated. The increase in exosome release supports the emerging view that PDT can modulate tumor–immune crosstalk and influence the TME beyond direct cytotoxicity [43–45]. Although exosome release following PDT exerts adjuvant antitumor effects, these vesicles also propagate oncogenic signals within tumor cells and help create pre-metastatic niches [42]; therefore, we require detailed characterization of their molecular cargo (ideally in a tumor-specific manner) to fully understand their contribution to post-PDT outcomes.

Collectively, these results demonstrate that ZnPc–PGA$_{20}$ and ZnPc–PGA$_{200}$ can integrate multiple functional modalities: they allow intrinsic NIR fluorescence for real-time monitoring, exhibit efficient endo-lysosomal uptake and retention, and prompt cytotoxicity in GBM cells. Additionally, the ability of ZnPc–PGA$_{20}$ to support light-activated ROS generation and modulate extracellular vesicle dynamics under PDT conditions may unlock new opportunities for immunomodulatory or combination therapeutic strategies. These features position ZnPc–PGA$_{20}$ and ZnPc–PGA$_{200}$ as advanced multifunctional theranostics tailored for precision GBM intervention.

2.3 | Advanced 3D Models Reveal Architecture- and Oxygen-Dependent PDT Efficacy in GBM

Tumors such as GBM exhibit spatial and metabolic heterogeneity, including the coexistence of proliferative rims, invasive peripheries, and hypoxic or necrotic cores, driven by rapid proliferation, poor vascularization, and high oxygen consumption [47]. Hypoxic zones associate with enhanced resistance to chemotherapy and radiotherapy, metabolic rewiring, and increased invasiveness [48, 49] and pose limitations for PDT, which relies on molecular oxygen to generate cytotoxic singlet oxygen ($^1O_2$) via type-II photochemical mechanisms. While oxygen depletion directly suppresses ROS generation, reducing therapeutic efficacy [50], most in vitro PDT studies employ normoxic conditions in 2D monolayer cultures, thereby overestimating therapeutic efficacy. Physiologically relevant 3D models that incorporate the ECM and oxygen gradients provide a more accurate assessment of nanotherapeutic performance by recapitulating the TME's structural and biochemical complexity [51].

To assess how ZnPc–PGA$_{20}$ and ZnPc–PGA$_{200}$ perform in such environments, we first validated their PDT efficacy in a 3D collagen-embedded GBM cell model – a transitional platform between conventional 2D monolayers and more advanced organotypic models. PDT induced by high light doses (70 J cm^{-2}) in A172 and U251MG cells revealed that ZnPc–PGA$_{20}$ maintained consistent IC$_{50}$ values between 2D and 3D culture conditions (Figure S16, Tables S4 and S5), indicating no significant loss of function. In contrast, ZnPc–PGA$_{200}$ displayed reduced efficacy under 3D culture conditions, due to diffusion limitations imposed by the collagen matrix, which acts as a physical barrier and mimics ECM-like environments.

To better replicate GBM pathophysiology, we utilized a barrier-free GBM-on-a-chip platform (Be-Gradient, Beonchip SL), which establishes oxygen and nutrient gradients via ECM embedding and spatially controlled perfusion (Figure 4A) [52, 53]. The device employed comprises a central chamber containing collagen-embedded tumor cells and two flanking microchannels that enable diffusion from opposite sides, providing an effective platform for evaluating diffusion-limited therapies [52–54]. Fabricated from cyclic olefin polymer (a gas-impermeable material), the platform facilitates oxygen gradients based on cellular oxygen consumption, unlike conventional polydimethylsiloxane-based systems. This approach reproduces GBM microenvironmental features, including necrotic/hypoxic cores, hypoxic perinecrotic

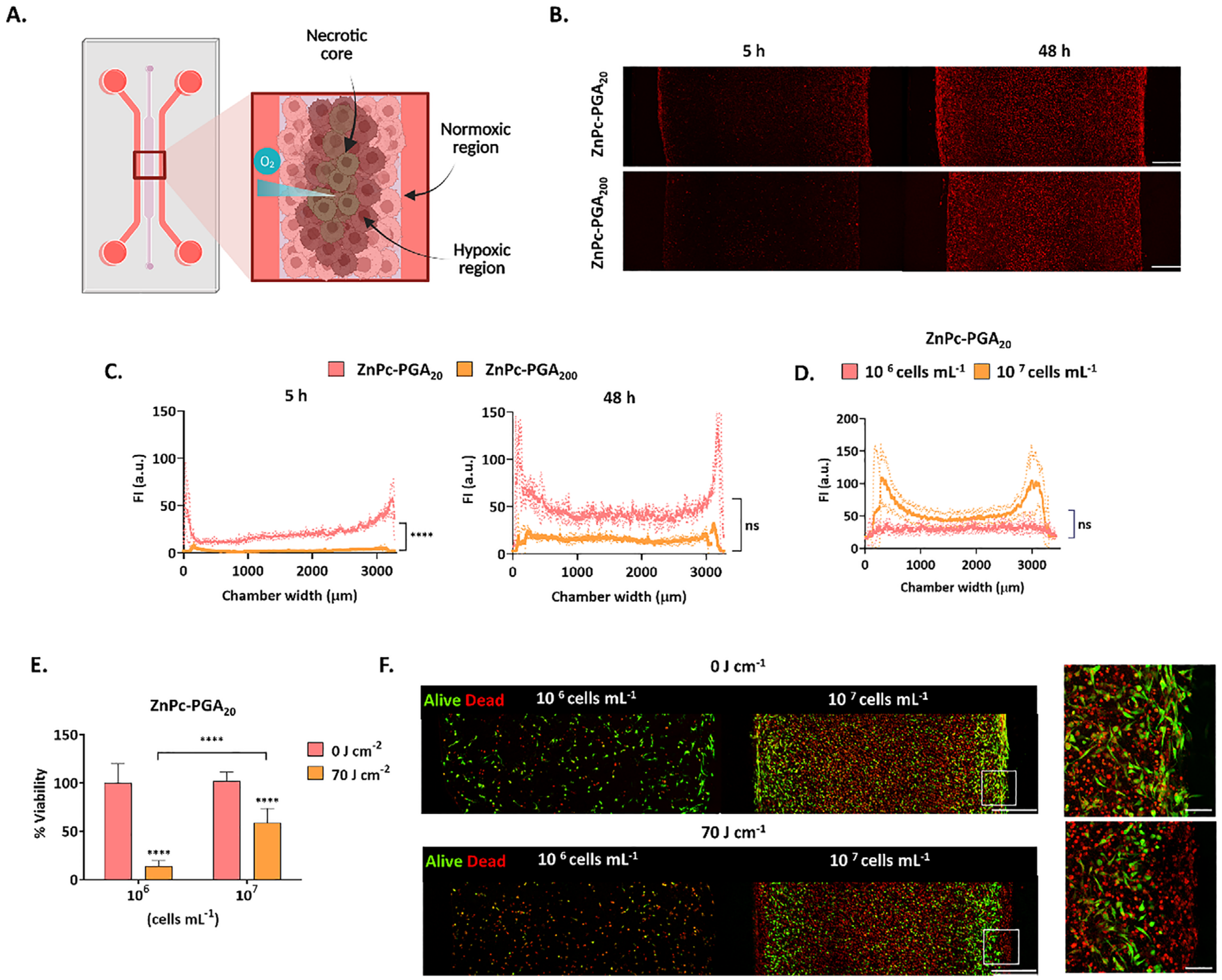

FIGURE 4 | Diffusion kinetics, cellular uptake, and PDT efficacy of ZnPc–PGA$_{20}$ and ZnPc–PGA$_{200}$ in a 3D GBM organ-on-chip model under normoxic and hypoxic conditions. (A) Schematic illustration of the microfluidics-based GBM-on-a-chip platform. *Created with BioRender.com*. (B) Confocal fluorescence images of the spatiotemporal distribution of ZnPc–PGA$_{20}$ and ZnPc–PGA$_{200}$ (10 µM ZnPc equivalents) after administration to a GBM-on-a-chip platform at 5 h (left) and 48 h (right) post-perfusion (A172 cells). (C) Quantitative analysis of fluorescence intensity (FI) in aribtrary units (a.u.) through the chamber width of the chip after 5 h (left, $n = 4$) and 48 h (right, $n = 2$), comparing ZnPc–PGA$_{20}$ and ZnPc–PGA$_{200}$ uptake. A two-way ANOVA test compared FI values at the chamber center between ZnPc–PGA$_{20}$ and ZnPc–PGA$_{200}$ at both time points; data represented as mean ± SD. Significance reported as $^{****}p \leq 0.0001$, ns = not significant. (D) Spatial fluorescence profiles of ZnPc–PGA$_{20}$ in GBM-on-a-chip platforms seeded with low (10^{6} cells mL^{-1}) or high (10^{7} cells mL^{-1}) A172 cell densities. Two-way ANOVA; ($n = 4$–7) data represented as mean ± SD. ns = not significant. (E) PDT response following ZnPc–PGA$_{20}$ treatment (10 µM ZnPc equivalents) and irradiation (660 nm, 70 J cm^{-2}) with non-irradiated controls (0 J cm^{-2}) under cell densities that support hypoxia (10^{7} cells mL^{-1}) and normoxia (10^{6} cells mL^{-1}). Two-way ANOVA test comparing cell viability assessed with Presto Blue, comparing PDT efficacy to the non-irradiated control, and between hypoxic and normoxic conditions; $n = 2$–3, mean ± SD. Significance reported as $^{****}p \leq 0.0001$. (F) Fluorescence microscopy images showing live (Calcein-AM, green) and dead (ZnPc-PGA$_{20}$ fluorescence, red) cells for non-irradiated controls (Left) and post-PDT examples (right) at low (10^{6} cells mL^{-1}; top) and high (10^{7} cells mL^{-1}; bottom) A172 cell densities. Scale bars: overview = 500 µm; Magnified regions = 100 µm.

zones, and oxygen-rich peripheries, which closely match in vivo architectures. We incorporated the hypoxia-sensitive dye ImageIT Red into the hydrogel and culture medium (to ensure uniform distribution) to monitor oxygen levels inside the microfluidic device (the dye fluoresces more as oxygen decreases to <5% O_2). High cell densities (10^{7} cells mL^{-1}) led to rapid oxygen depletion toward the chamber center, forming a hypoxic core with the highest FI at day 3 (30 a.u.); in contrast, low-density cultures (10^{6} cells mL^{-1}) maintained uniform oxygenation over 3 days, as indicated by stable FI (10 a.u.) (Figures S17A,B).

We investigated whether nanocarrier size influenced diffusion and uptake by perfusing the GBM-on-a-chip platforms containing A172 cells at 10^{7} cells mL^{-1} with ZnPc–PGA$_{20}$ or ZnPc–PGA$_{200}$ (10 µM ZnPc equivalents) through lateral channels by monitoring ZnPc-PGA FI. Confocal fluorescence images of transverse sections of the chamber at 5 and 48 h (Figure 4B) revealed significantly higher uptake of ZnPc–PGA$_{20}$ at 5 h (Figure 4C, comparing FI of ZnPc–PGA$_{20}$ or ZnPc–PGA$_{200}$ at the chamber center; $^{****}p < 0.0001$), reflecting the more rapid penetration of ZnPc–PGA$_{20}$. After 48 h, ZnPc–PGA$_{20}$ and ZnPc–PGA$_{200}$ reached the chamber center with no statistically significant difference in FI (Figure 4C), demonstrating that ZnPc–PGA$_{200}$, despite slower initial diffusion, achieves a distribution equilibrium comparable to that of ZnPc–PGA$_{20}$ in this dynamic 3D microenvironment. We observed increased fluorescence at chamber margins (directly in contact with the ZnPc-PGA-containing media), with a more pronounced effect for ZnPc-PGA$_{20}$, likely due to local nanocarrier accumulation and the more elongated morphology of cells in these regions, both of which contribute to a higher fluorescence signal.

To determine whether cell density (governing oxygen gradients) affects nanocarrier diffusion, we compared ZnPc–PGA$_{20}$ fluorescence in GBM-on-a-chips seeded with low (10^6 cells mL^{-1}) or high (10^7 cells mL^{-1}) densities (Figure 4D). Crucially, we failed to observe significant differences in FI from ZnPc–PGA$_{20}$ in the chamber center between densities (Figure 4D), confirming that cellular crowding does not restrict ZnPc–PGA$_{20}$ diffusion. While we made this comparison with ZnPc–PGA$_{20}$, the complete spatial distribution observed with ZnPc–PGA$_{200}$ after 48 h suggests that size and exposure time, rather than cell density, govern nanocarrier behavior in the chip (Figure 4C). These data underscore the capacity of ZnPc–PGA$_{20}$ and ZnPc–PGA$_{200}$ to reach equilibrium across the 3D matrix, despite differences in initial diffusion kinetics. While displaying slower early penetration (particularly in static ECM-rich models), ZnPc–PGA$_{200}$ achieves full spatial coverage in the dynamic GBM-on-a-chip environment and therefore suits further downstream applications.

The ability of ZnPc–PGA$_{20}$ to rapidly achieve uniform spatial distribution, even within densely packed and ECM-rich tumor-like matrices, enables a more accurate assessment of PDT performance across regions with distinct oxygenation levels. This distinction remains essential; incomplete accumulation in hypoxic cores can lead to misattributed therapeutic resistance. Accordingly, we selected ZnPc–PGA$_{20}$ for the comparative evaluation of PDT under hypoxic versus normoxic conditions, given that ZnPc–PGA$_{20}$ retained comparable potency in 2D and 3D cultures (no significant differences in IC$_{50}$ values), whereas ZnPc–PGA$_{200}$ displayed a marked loss of efficacy in 3D cultures, consistent with slower diffusion/penetration through the hydrogel matrix. We incubated the GBM-on-a-chip with 10 µm ZnPc–PGA$_{20}$ (ZnPc equivalents) and irradiated at 660 nm (70 J cm^{-2}) (non-irradiated chips [0 J cm^{-2}] served as controls for 100% cell viability). We discovered that irradiation following ZnPc–PGA$_{20}$ treatment induced a significant decrease in cell viability when culturing cells at densities of 10^6 cells mL^{-1} (normoxia) and 10^7 cells mL^{-1} (hypoxia) compared to the non-irradiated control (both $^{****}p \leq 0.0001$); however, hypoxic conditions significantly reduced the degree of PDT-induced cytotoxicity ($^{***}p < 0.0001$) (Figure 4E). Of note, the GBM-on-a-chip platform reproduces distinct tumor regions (such as the necrotic core, proliferative margins, and diffuse invasive zones) and, as such, allows spatial mapping of PDT response; therefore, we performed fluorescence imaging to map the spatial distribution of therapeutic response. The retention of ZnPc fluorescence by non-viable cells enabled the identification of dead (ZnPc-PGA, red) and live (Calcein-AM, green) cells. As expected, cell death predominantly occurred in the well-oxygenated proliferative margins of irradiated chips, whereas cells residing in the hypoxic regions, despite comparable nanocarrier uptake, remained resistant, consistent with the oxygen dependence of PDT (Figure 4F). This spatial pattern reflects the oxygen dependency of type-II PDT and validates hypoxia as a therapeutic barrier in GBM.

These results confirm that the densely packed architecture of the tumor core does not impede ZnPc–PGA$_{20}$ diffusion; however, hypoxia profoundly limits PDT efficacy, regardless of drug distribution, underscoring the need to incorporate physiologically relevant oxygen gradients into preclinical models and emphasizing the translational utility of the GBM-on-a-chip platform. Unlike traditional 2D or even static 3D models, this system enables spatiotemporal decoupling of delivery and efficacy, providing a realistic framework for dissecting molecular resistance mechanisms and biophysical constraints, such as interstitial diffusion, mass transport, and metabolic heterogeneity. These insights also support the development of combinatorial therapeutic strategies to overcome hypoxia-driven resistance in GBM, such as oxygen-generating biomaterials, hypoxia-activated prodrugs, and PDT, and highlight the value of 3D microfluidic platforms for advancing precision nanomedicine in solid tumors.

2.4 | Post-Polymerization Drug Conjugation of ZnPc-PGA Nanocarriers for Combination Therapy

ZnPc-PGA serves as a modular, multifunctional scaffold that supports post-polymerization modification, enabling the covalent attachment of chemotherapeutic agents alongside the PDT and imaging capabilities of the phthalocyanine core. To explore utility in combination therapies, we functionalized the pendant carboxylic groups of PGA arms with paclitaxel (PTX), a clinically validated microtubule-stabilizing agent widely used in cancer treatment and amenable to well-established conjugation chemistries [55, 56]. Notably, since both ZnPc–PGA$_{20}$ and ZnPc–PGA$_{200}$ displayed comparable physicochemical and biological profiles in earlier studies, synthetic versatility primarily guided the choice of polymer length at this stage. We selected the longer-armed ZnPc–PGA$_{200}$ for PTX conjugation, as this nanocarrier provided increased drug-loading capacity, greater steric accessibility, and improved solubilization of hydrophobic drugs. We covalently linked PTX via ester bonds, yielding a stable conjugate – ZnPc–PGA$_{200}$–PTX – with a fixed ZnPc:PTX molar ratio of 1:2, a drug loading of 1.2 mol% (as determined by ^{1}H-NMR) (Figure 5A; Supplementary Material, Scheme S2; Figure S18), and a percentage of free-drug of 0.3 wt.% (compared to total wt.% drug loading, as determined by LC-MS/MS).

Spectroscopic and scattering analyses revealed that PTX conjugation significantly altered the supramolecular architecture of ZnPc–PGA$_{200}$ (Figure 5B). UV–vis spectroscopy revealed a sharper and red-shifted Q-band (∼714 nm) in ZnPc–PGA$_{200}$–PTX compared to ZnPc–PGA$_{200}$, indicative of reduced π–π stacking interactions and partial disaggregation of ZnPc chromophores (Figure 5B). This reduction in excitonic coupling suggests an increased average distance between ZnPc units, likely arising from steric interference imposed by the bulky PTX moieties. DLS measurements further supported this interpretation, revealing an increase in the Rh value to 37.9 ± 4.4 nm for ZnPc–PGA$_{200}$–PTX compared to ZnPc–PGA$_{200}$ (Rh = 19 ± 4 nm; Table 1), indicating an expansion of the solvated outer shell. This finding

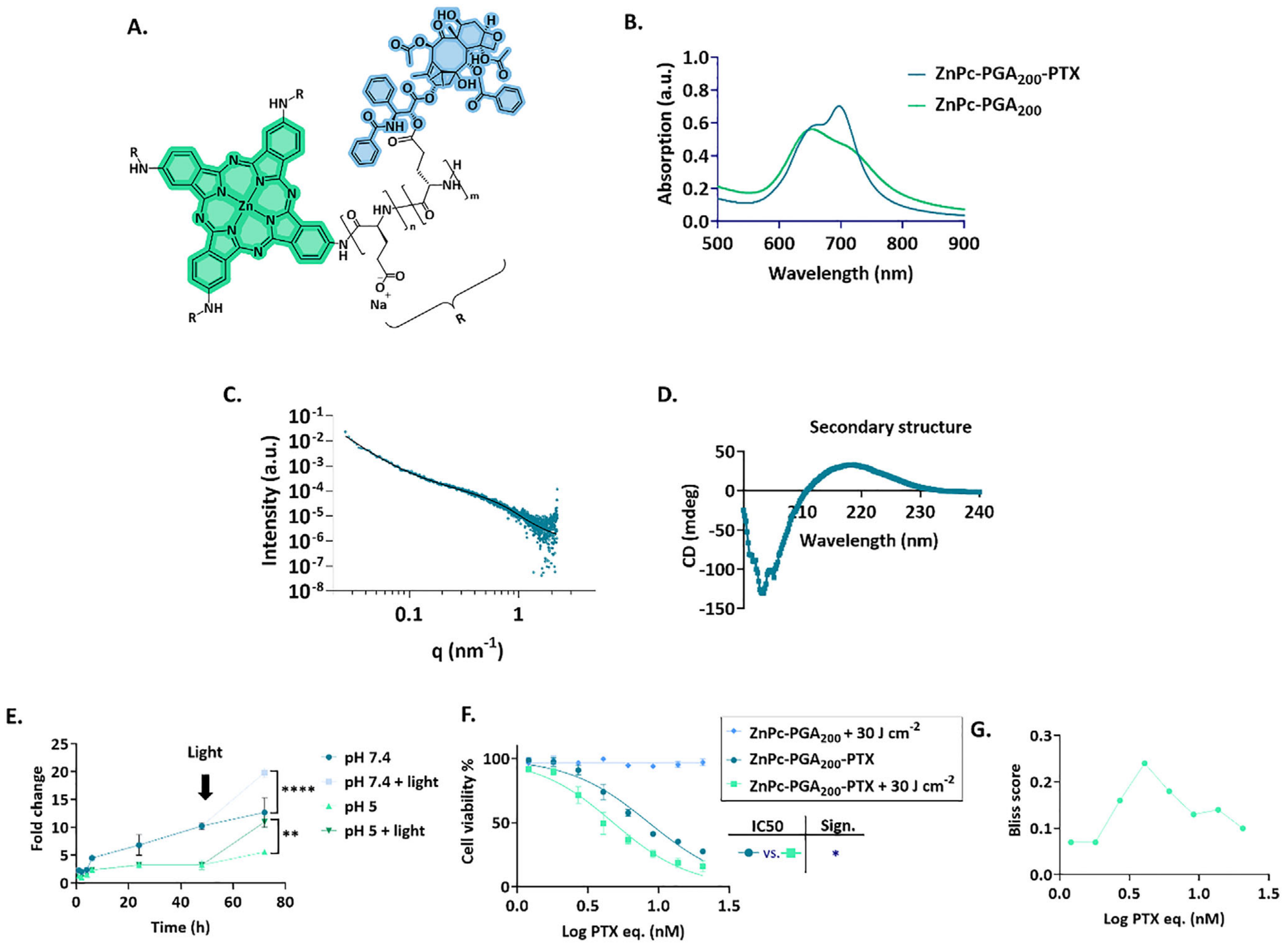

FIGURE 5 | ZnPc-PGA nanocarriers support combination therapy-based tumor treatment in GBM cells. (A) Schematic representation of ZnPc-PGA$_{200}$-PTX. (B) Comparison of UV–vis absorbance spectra of ZnPc-PGA$_{200}$ and ZnPc-PGA$_{200}$-PTX in water. (C) SAXS profile of ZnPc-PGA$_{200}$-PTX, displaying intensity as a function of the scattering momentum transfer, q ($q = 4\pi \sin \theta / \lambda$). (D) CD spectra of ZnPc-PGA$_{200}$-PTX in PBS. (E) PTX release at pH 5 and 7.4 from ZnPc-PGA$_{200}$-PTX. Data represented as fold change of the percentage of free-drug normalized to total drug loading for each time point relative to time 0 h. Two-way ANOVA test compared experimental values to the respective non-irradiated control; $n = 2$, mean ± SEM. Significance reported as $^{**}p \leq 0.01$, $^{****}p \leq 0.0001$. (F) U251MG cell viability determined by MTS assay after exposure to ZnPc-PGA$_{200}$-PTX, evaluated under dark conditions (IC$_{50}$ = 8.6 nM PTX eq) and upon light irradiation (30 J cm^{-2}, IC$_{50}$ = 4.8 nM PTX eq). A *T*-test compared IC$_{50}$ values; $n = 3$, data represented as mean ± SEM. Significance reported as $^{*}p \leq 0.05$. (G) Synergism scores calculated using the Bliss model from the dose-response curves by inducing photodynamic therapy in U251 cells (30 J/cm^2) and ZnPc-PGA$_{200}$-PTX alone/in combination. Bliss score values of < 0 indicate antagonism, 0-to-0 indicate additivity (lack of synergism/antagonism), and > 0 indicate synergism.

aligns with the notion of a more hydrated, flexible corona resulting from the incorporation of hydrophobic PTX, which disrupts the compact peripheral chain packing. Notably, despite this size increase, ZnPc–PGA$_{200}$–PTX preserved its characteristic anionic surface properties, maintaining a markedly negative ζ-potential (−29.4 ± 1.7 mV), which supports colloidal stability and suggests that PTX grafting does not compromise the electrostatic profile of the PGA scaffold. Conversely, SAXS analysis revealed a slightly lower Rg value (5.6 ± 0.1 nm) for ZnPc–PGA$_{200}$–PTX (Figure 5C) compared to ZnPc–PGA$_{200}$ (Rg = 7.8 ± 0.8 nm; Table 1). This apparent discrepancy between DLS and SAXS may stem from their differential sensitivities: while DLS captures changes in the hydrodynamic volume influenced by surface hydration and molecular flexibility, SAXS probes the electron density distribution of the compact core. The decrease in Rg suggests preservation or slightly enhanced core compaction, despite increased peripheral flexibility.

Consistent with this hypothesis, CD spectra confirmed that PGA chains retained their random-coil conformation after PTX conjugation (Figure 5D). Together, these findings suggest that PTX conjugation perturbs the peripheral architecture, increasing hydration and flexibility, while maintaining the integrity of the central supramolecular cylindrical core. The steric bulk of PTX introduces additional spacing between ZnPc chromophores, thereby alleviating self-quenching, as evidenced by the UV–vis absorbance spectra. We evaluated the colloidal stability of ZnPc–PGA$_{200}$–PTX by nanoparticle tracking analysis (NTA) after incubation in PBS or PBS supplemented with 10% FBS at 37°C over 24 h (Figure S19). ZnPc–PGA$_{200}$–PTX assemblies remained stable in both types of media, displaying minimal changes in average particle size and particle concentration over time. These results indicate that ZnPc–PGA$_{200}$–PTX maintained supramolecular integrity under physiologically relevant conditions and that the presence of serum proteins did not induce significant aggregation or disassembly of the aggregates. These slight changes likely reflect limited dynamic rearrangement of the assemblies rather than structural destabilization.

To evaluate drug release kinetics from ZnPc–PGA$_{200}$–PTX, we investigated PTX release profiles in 20 mᴍ sodium acetate buffer (pH 5) and Dulbecco's phosphate-buffered saline (DPBS) (pH 7.4), simulating acidic TME and physiological plasma conditions, respectively. We incubated ZnPc–PGA$_{200}$–PTX in both buffers at 37°C under agitation for 72 h; at the 48 h time point, we irradiated the corresponding samples to mimic treatment conditions in cell assays. We conjugated PTX via esterification of the pendant carboxylic acid groups of the PGA backbone, yielding ZnPc-PGA–PTX prodrugs with dual pH- and light-responsive properties. As shown in Figure 5E, we observed negligible but detectable PTX release in the absence of light under both conditions, consistent with the inherent susceptibility of ester linkages to slow hydrolytic cleavage in aqueous environments. Similar behavior has been reported for related polymer–drug conjugates, where gradual hydrolysis contributes to baseline release profiles [56, 57]. Upon light exposure (70 J cm^{-2} after a 48 h incubation), we observed a significant enhancement in PTX release, with an approximately two-fold increase in cumulative release compared to non-irradiated controls (Figure 5E). We attribute this effect to the generation of ROS by the ZnPc core, which promotes oxidative cleavage of the ester linkage. Notably, we observed more pronounced release at pH 7.4 than at pH 5 ($^{****}p \leq 0.0001$ vs $^{**}p \leq 0.01$), likely reflecting increased ROS stability and diffusion under neutral conditions, whereas acidic environments may favor ROS quenching or reduced reactivity.

Although light irradiation also enhanced release at pH 5, the lower magnitude suggests a less efficient process, potentially involving a combination of acid-catalyzed hydrolysis and ROS-mediated cleavage. Overall, these results demonstrate that ZnPc–PGA$_{200}$–PTX functions as a dual-responsive prodrug system, in which light-triggered acceleration of drug release complements baseline hydrolysis. This phototriggered, pH-tuned release behavior mirrors observations for other PGA-based ester-linked conjugates [58] and highlights the advantage of integrating light-activatable prodrug strategies into a ZnPc-PGA nanocarrier.

We next evaluated the biological performance of ZnPc–PGA$_{200}$–PTX in U251MG cells in the absence of light and under PDT conditions. Treatment with ZnPc–PGA$_{200}$–PTX in the absence of light resulted in concentration-dependent cytotoxicity, attributable to PTX's chemotherapeutic activity; however, PDT conditions (irradiation at 660 nm, 30 J cm^{-2}) significantly enhanced cytotoxicity (Figure 5F), with IC$_{50}$ values significantly decreasing from 8.6 ± 1 nᴍ (dark) to 4.8 ± 0.6 nᴍ (light), normalized to PTX equivalents ($^{*}p \leq 0.05$). These results highlight a synergistic interaction between PDT and PTX, consistent with prior findings in solid tumors, in which PDT-induced oxidative stress sensitizes cancer cells to microtubule inhibitors, thereby amplifying apoptosis [59–61].

To quantitatively assess the interaction between ZnPc-mediated PDT and PTX, we evaluated the cytotoxic effect of each treatment under identical experimental conditions. Within the concentration range evaluated, ZnPc-mediated PDT alone produced minimal cytotoxicity (Figure 5F); therefore, we evaluated drug interaction using the Bliss independence model [62]. We calculated the expected additive effect from the cytotoxicity of each monotherapy at equivalent ZnPc concentrations and compared these values with the observed response of the combination. We observed positive Bliss score values across all tested concentrations, indicating a synergistic interaction between ZnPc-mediated PDT and PTX (Figure 5G; Table S6).

Of note, the covalent integration of both therapeutic modalities into a single polypeptide chain ensures a fixed, reproducible ratio between the photosensitizer and the chemotherapeutic agent, simplifying formulation and enabling simultaneous delivery of both payloads to the desired site. While further optimization of the ZnPc-to-PTX ratio could enhance synergy, these findings, taken together, support the design of site-specific, on-demand drug delivery systems with maximal control under physiological conditions, offering particular relevance for GBM therapy when combined with photodynamic activation.

2.5 | Non-Invasive Intranasal Administration of ZnPc-PGA Nanocarriers Safely Achieves Safe and Efficient Brain Uptake in Healthy Mice

The BBB represents a significant barrier to GBM-directed nanomedicines, significantly restricting CNS delivery following systemic administration [4]. We explored intranasal administration to overcome this problem, given that our previous work demonstrated that star-shaped PGAs successfully circumvent the BBB and reach the brain [63].

2.5.1 | Crosslinked ZnPc-PGA-based Supramolecular Assemblies Provide Enhanced Stability and Mucoadhesion Required for Intranasal Brain Delivery

To support mucosal adhesion and prolong residence time in the nasal cavity, we incorporated ZnP-cPGA nanocarriers into an HA-CP hydrogel delivery system [58] to enhance permeation and provide depot-like retention. To further enhance the structural stability and nasal residence time of ZnPc-PGA nanocarriers, we designed a crosslinked nanocarrier formulation (ZnPc–PGA$_{200}$–CL) based on disulfide bridge formation between pendant groups on PGA arms. Building on our previous studies using star-shaped PGA-based platforms that enhance mucosal adhesion via thiol–disulfide exchange with mucin glycoproteins [64], we aimed to increase the formulation's mucoadhesive potential, thereby promoting prolonged retention at the nasal epithelium and enhanced interaction with mucosal barriers during nose-to-brain delivery.

The synthetic route for ZnPc–PGA$_{200}$–CL followed a two-step procedure (Scheme S3). We first modified ZnPc–PGA$_{200}$ with pyridyl disulfide (PD) via direct coupling to free carboxyl groups on PGA side chains, yielding ZnPc–PGA$_{200}$–PD (9 mol.% PD) (Figure S20), which introduced thiol-reactive handles for subsequent crosslinking. We then subjected the PD-functionalized nanocarrier to nanoprecipitation in the presence of hexa(ethylene glycol) dithiol, forming reversible disulfide crosslinks between polypeptide chains. This process yielded the final ZnPc–PGA$_{200}$–CL nanostructure (Figure 6A), which displayed a stable network

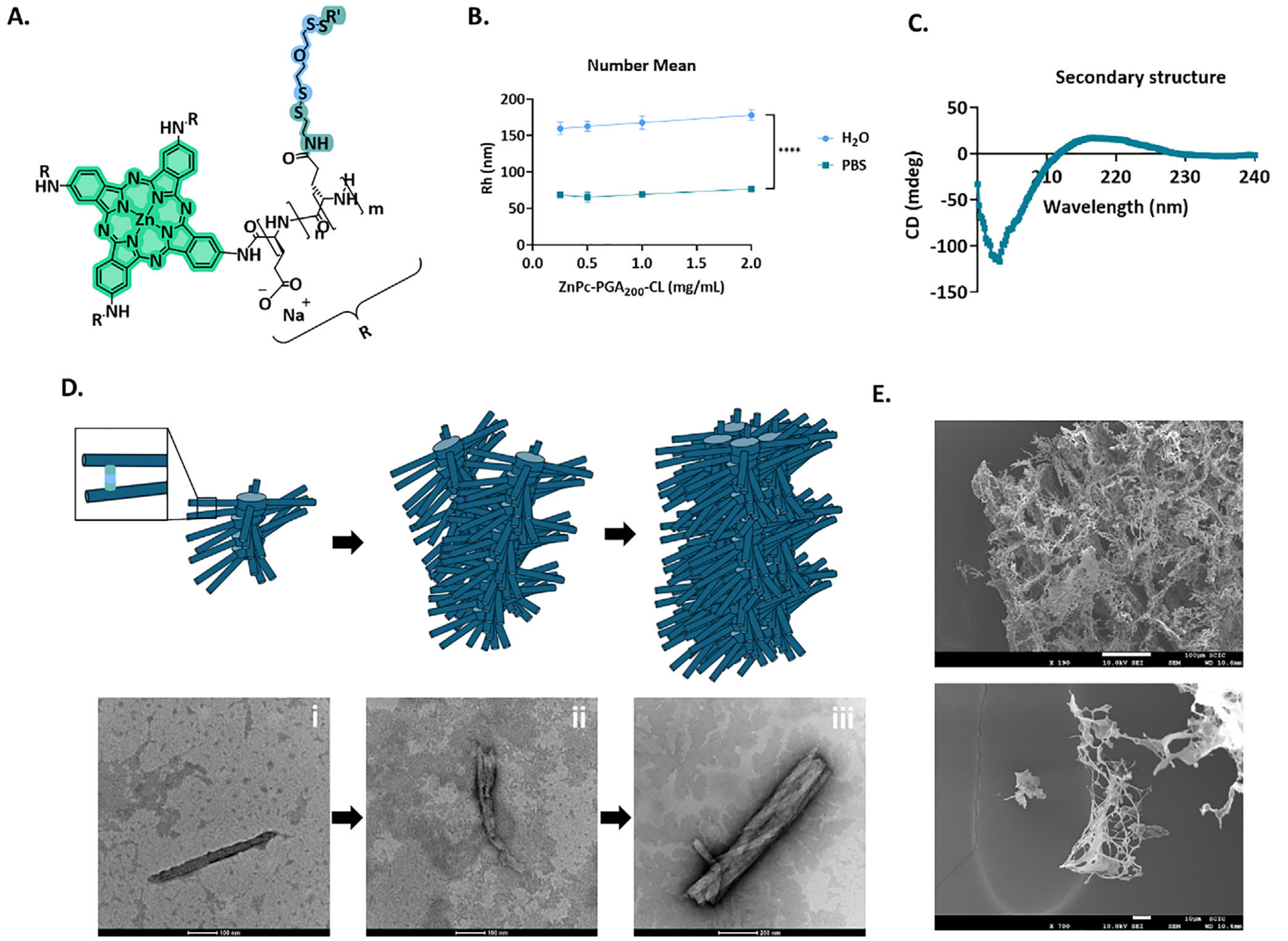

FIGURE 6 | Disulfide-crosslinked ZnPc-PGA$_{200}$-CL forms supramolecular assemblies with enhanced stability for intranasal permeation and brain delivery. (A) Schematic representation of ZnPc-PGA$_{200}$-CL. (B) DLS analysis of ZnPc-PGA$_{200}$-CL in water and PBS at a range of concentrations (0.125 to 2 mg mL^{-1}). Two-way ANOVA test compared the hydrodynamic size between water and PBS at each concentration; $n = 6$, number mean ± SD. Significance reported as ****$p \leq 0.0005$. (C) CD spectra of ZnPc-PGA$_{200}$-CL in PBS. (D) TEM images depicting the formation of cylindrical structures for ZnPc-PGA$_{200}$-CL at 0.25 mg mL^{-1}. Schematic illustration of the proposed bundling process, from single fibers to higher-order assemblies, and the representative structures observed in the TEM samples, including (i) individual fibers, (ii) the association of two fibers, and (iii) bundles formed by the lateral assembly of multiple fibers. (E) Scanning electron micrographs of ZnPc-PGA$_{200}$-CL displaying filament-like networks; upper image, scale bar = 100 µм; lower image, scale bar = 10 µм.

maintained by disulfide bridges responsive to reductive environments, allowing stimuli-responsive disassembly in intracellular compartments.

We analyzed ZnPc–PGA$_{200}$–CL by DLS in water and PBS over a concentration range (0.125–2 mg mL^{-1}) to characterize colloidal behavior; we observed significant differences in Rh values in water (Rh = 167 nm) and PBS (Rh = 70 nm) for all concentrations (Figure 6B, ****$p \leq 0.0001$), while maintaining the negative ζ-potential (−31.4 ± 1.0 mV). We attribute this size contraction under the saline conditions (PBS) to ionic strength-induced screening of electrostatic repulsion and disruption of loose aggregates. Notably, the hydrodynamic size remained stable upon dilution in PBS, indicating colloidal integrity and resistance to dissociation, a crucial advantage for mucosal retention and transport. TEM confirmed that ZnPc–PGA$_{200}$–CL retained the fiber-like supramolecular architecture of ZnPc–PGA$_{200}$ (Figure 6C). These cylindrical structures observed in TEM, typical of phthalocyanine assemblies, revealed greater robustness after crosslinking than ZnPc–PGA$_{200}$, forming thicker, laterally associated bundles that reflect enhanced supramolecular cohesion (Figure 6D). Similar behaviors have been reported for other peripherally functionalized phthalocyanines, where side-chain interactions induce multifilament assembly and improved structural stability [65]. Scanning electron microscopy analysis further supported the enhanced structural stability achieved through disulfide crosslinking; while we did not detect isolated cylindrical filaments characteristic of ZnPc–PGA$_{200}$ (Figure S11), ZnPc–PGA$_{200}$–CL formed a more reticulated, filament-like network (Figure 6E).

We further assessed the colloidal stability of ZnPc–PGA$_{200}$–CL by NTA after incubation in PBS or PBS supplemented with 10% FBS at 37°C (Figure S21). While particle size remained relatively stable in PBS, with minimal variation in particle concentration, incubation with 10% FBS led to a slight decrease in average particle size at 24 h, accompanied by an increase in particle number, suggesting partial disaggregation of the supramolecular assemblies. Overall, this behavior remains consistent with interactions between serum proteins and the disulfide crosslinks, which may promote dissociation of the assemblies.

In summary, structural and colloidal analyses confirmed that ZnPc–PGA$_{200}$–CL forms robust cylindrical assemblies with stable hydrodynamic size across physiological conditions, supporting the suitability of this crosslinked supramolecular assembly for prolonged nasal retention and controlled intracellular disassembly.

2.5.2 | Biodistribution Profiles Confirm Efficient Brain Targeting of ZnPc-PGA Nanocarriers after Intranasal Delivery

We next investigated the in vivo biodistribution of ZnPc–PGA$_{20}$, ZnPc–PGA$_{200}$, and ZnPc–PGA$_{200}$–CL after intranasal administration to healthy Balb/c mice, leveraging the intrinsic fluorescence of ZnPc for non-invasive tracking and the HA-CP hydrogel delivery system. We assessed biodistribution at 4, 24, and 48 h post-administration via ex vivo fluorescence imaging using the IVIS Lumina X5 system (Figure 7), with quantification expressed as total radiant efficiency (TRE) normalized to tissue weight. We administered ZnPc–PGA$_{20}$, ZnPc–PGA$_{200}$, and ZnPc–PGA$_{200}$–CL at 30 µg ZnPc equivalents per mouse and detected all three formulations in the olfactory mucosa and deeper brain regions, confirming their ability to cross the nasal epithelium and access CNS structures (Figure 7A–C). The detection of ZnPc-derived fluorescence at the level of the nasal mucosa suggests that assemblies underwent at least partial disassembly during or prior to epithelial transit, indicating that structural reorganization of the nanocarrier may already occur within the enzymatically active nasal microenvironment before reaching deeper brain regions. These results support the activation of direct nose-to-brain transport routes, including perineural and transcellular pathways along the olfactory and trigeminal nerves, thereby enabling delivery of intact nanocarriers into CNS compartments while bypassing the BBB.

A more detailed analysis of the olfactory mucosa revealed similar kinetic profiles among ZnPc–PGA$_{20}$, ZnPc–PGA$_{200}$, and ZnPc–PGA$_{200}$–CL (Figure 7A). Administration of ZnPc–PGA$_{20}$ and ZnPc–PGA$_{200}$ prompted a moderate increase in fluorescence from 4 to 24 h, followed by a gradual decline at 48 h, consistent with transient mucosal retention and progressive transport toward the brain. While maintaining this kinetic profile, ZnPc–PGA$_{200}$–CL administration resulted in higher FI at all time points compared with ZnPc–PGA$_{20}$ and ZnPc–PGA$_{200}$, although this difference did not reach statistical significance. However, we did observe a statistically significant decrease in fluorescence for ZnPc–PGA$_{200}$–CL between 24 and 48 h (*$p < 0.05$), indicating enhanced initial adhesion to the mucosal surface. This behavior aligns with the expected mucoadhesive properties of the disulfide-crosslinked network, which can promote tighter interactions with mucin and reduced mucociliary clearance [63]. Nevertheless, the consistently higher fluorescent signal from ZnPc–PGA$_{200}$–CL in the mucosa did not reach statistical significance compared with the other formulations due to inter-individual variability. We observed low fluorescence signals in the olfactory bulbs for ZnPc–PGA$_{20}$, ZnPc–PGA$_{200}$, and ZnPc–PGA$_{200}$–CL, indicating rapid diffusion throughout the brain parenchyma (Figure 7B). ZnPc–PGA$_{200}$–CL administration associated with a significant peak at 4 h compared to ZnPc–PGA$_{20}$ ($p < 0.05$), although not relative to ZnPc–PGA$_{200}$, likely owing to variability within the latter group. This transient peak may reflect the higher mucosal depot effect of the crosslinked formulation, enabling a more concentrated early flux toward the bulbs. In the brain, administration of ZnPc–PGA$_{20}$ resulted in a limited increase in fluorescence between 4 and 24 h, with a significant difference by 48 h (Figure 7C). ZnPc–PGA$_{200}$ administration led to maximal fluorescence at 24 h, which remained stable through 48 h (Figure 7C). ZnPc–PGA$_{200}$–CL administration led to a more linear, progressive increase over time, indicative of sustained release from the mucosal depot formed by the crosslinked architecture (Figure 7C). Notably, despite these kinetic differences, all ZnPc–PGA$_{20}$, ZnPc–PGA$_{200}$, and ZnPc–PGA$_{200}$–CL converged toward similar fluorescence intensities at 48 h, indicating that overall brain accumulation at later time points remained comparable. Collectively, these data highlight that the enhanced mucosal adhesion and early-phase retention of ZnPc–PGA$_{200}$–CL does not necessarily translate into greater total brain accumulation within the 48 h window considered. Further optimization of the density and distribution of disulfide moieties may enable a more favorable balance between mucosal adhesion and diffusion, potentially enhancing overall brain accumulation.

Looking at wider distribution, ZnPc–PGA$_{200}$ administration resulted in increased lung fluorescence compared with ZnPc–PGA$_{20}$ administration (*; $p < 0.05$) at 24 h, suggesting a slower clearance profile and a longer residence time for ZnPc–PGA$_{200}$ (Figure 7D). This behavior aligns with previous reports [66], indicating that nanocarrier size and aggregation state affect pulmonary retention and clearance kinetics, with larger or more structured nanocarriers displaying delayed elimination from the alveolar-capillary interface. Analysis of blood plasma, liver, and gastrointestinal tissues following ZnPc–PGA$_{20}$, ZnPc–PGA$_{200}$, and ZnPc–PGA$_{200}$–CL administration revealed no significant fluorescence at any examined time points (Figure 7E–G), indicating minimal systemic exposure and efficient compartmentalization of nanocarriers within the intended nasal and CNS regions. These findings suggest that the uncrosslinked or crosslinked nature of nanocarriers did not significantly influence systemic leakage or hepatic/gastrointestinal accumulation under the evaluated conditions. Notable differences emerged across other peripheral organs, reflecting the influence of nanocarrier architecture and supramolecular stabilization on biodistribution profiles. At 4 h post-administration, ZnPc–PGA$_{20}$ associated with significantly higher fluorescence in the kidneys (*** $p < 0.001$) compared to ZnPc–PGA$_{200}$ and ZnPc–PGA$_{200}$–CL (Figure 7H). This finding aligns with the smaller size and greater renal clearance propensity of ZnPc–PGA$_{20}$, supporting the hypothesis that lower-Mw nanocarriers undergo more efficient filtration and elimination via glomerular pathways. We observed a similar trend in the heart, where ZnPc–PGA$_{20}$ administration, despite its overall low accumulation, led to significantly higher fluorescence levels than ZnPc–PGA$_{200}$ and ZnPc–PGA$_{200}$–CL (Figure 7I), consistent with the more rapid systemic absorption and distribution of the smaller nanocarrier into highly vascularized tissues. In the

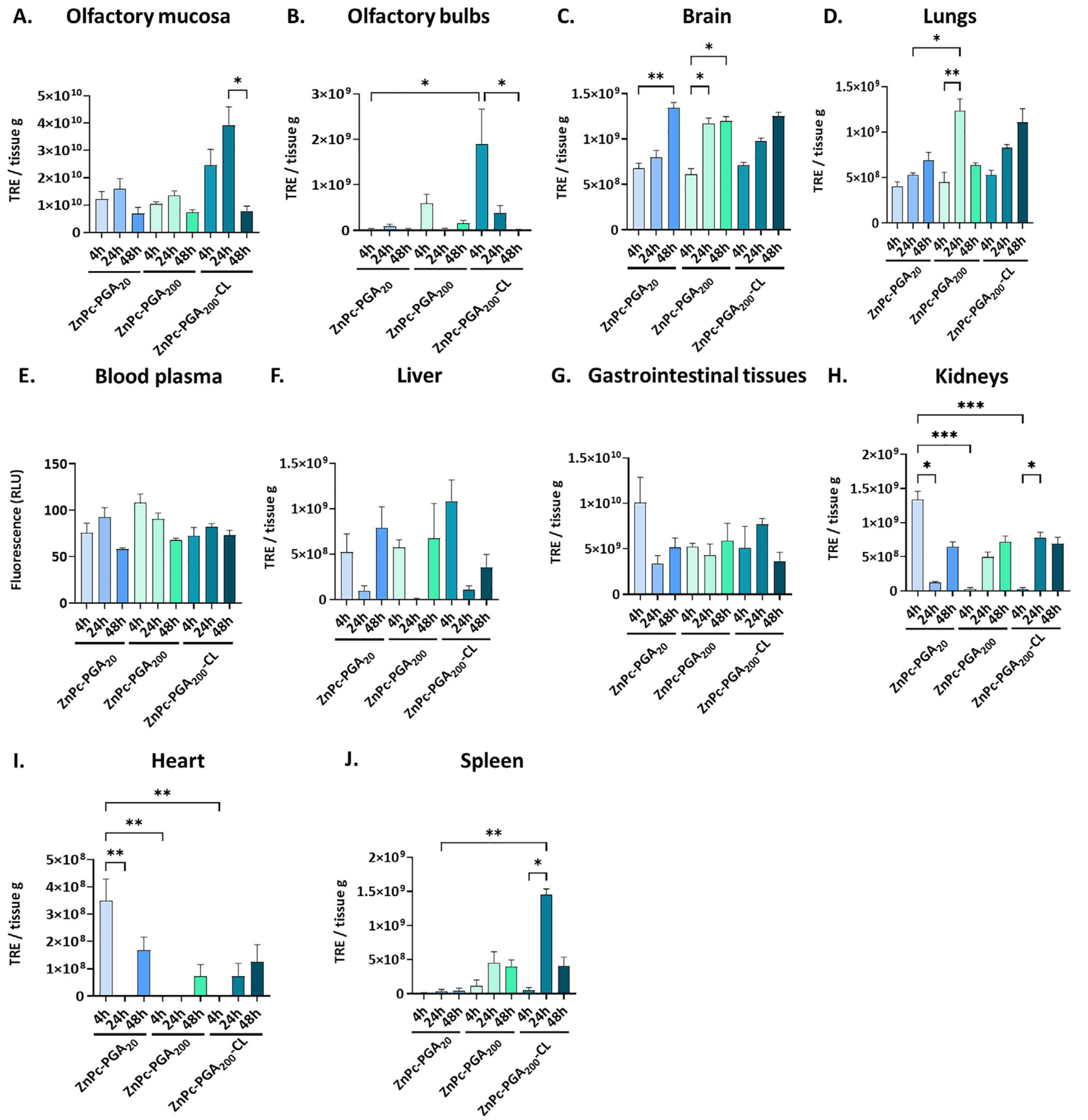

FIGURE 7 | In vivo biodistribution of ZnPc-PGA$_{20}$, ZnPc-PGA$_{200}$, and ZnPc-PGA$_{200}$-CL in healthy Balb/c mice after intranasal administration using an HA-CP hydrogel delivery system. Graphs depict analysis of the (A) olfactory mucosa, (B) olfactory bulbs, (C) brain, (D) lungs, (E) blood plasma, (F) liver, (G) gastrointestinal tissues, (H) kidneys, (I) heart, and (J) spleen. Fluorescence measured ex vivo using the IVIS Lumina X5 Imaging System. One-way ANOVA followed by a Kruskal–Wallis test compared differences for ZnPc-PGA$_{20}$, ZnPc-PGA$_{200}$, and ZnPc-PGA$_{200}$-CL across all time points and between time points for each compound. Data expressed as total radiant efficiency (TRE) per gram of tissue ($n = 5$, mean ± SEM). Significance reported as $^{*}p < 0.05$, $^{**}p < 0.01$, $^{***}p < 0.001$.

kidneys and heart, ZnPc–PGA$_{20}$ administration associated with a pronounced early peak in fluorescence (4 h), followed by partial or complete clearance and a subsequent increase at 48 h, indicating a bimodal distribution profile [67, 68]. Such dual-phase kinetics may reflect transient sequestration of ZnPc–PGA$_{20}$ by plasma proteins or other circulating macromolecules shortly after administration, temporarily reducing the fraction available for direct tissue uptake. As these reversible complexes dissociate over time, through dynamic protein corona exchange or competitive interactions with extracellular components, a second pool of free circulating ZnPc–PGA$_{20}$ may become available for redistribution, resulting in the delayed accumulation observed at 48 h. We also observed a striking difference in the spleen, where ZnPc–PGA$_{200}$–CL administration prompted significantly greater fluorescence at 24 h than ZnPc–PGA$_{20}$ or ZnPc–PGA$_{200}$ (Figure 7J).

This preferential splenic retention may be attributed to the increased colloidal stability and structural integrity of the disulfide-crosslinked assemblies, which enhance circulation time and promote passive accumulation in lymphoid tissues. In addition, their stabilized size within the ~10–250 nm range and negative surface charge favor lymph node-to-spleen transport [68, 69]. This behavior agrees with prior studies reporting that crosslinked nanocarriers preferentially localize to secondary lymphoid organs due to their reduced susceptibility to rapid degradation and their ability to engage phagocytic trafficking routes [68, 70]. The presence of stable multivalent structures in ZnPc–PGA$_{200}$–CL may facilitate stronger interactions with antigen-presenting cells and promote lymphoid uptake, thereby highlighting the potential of this platform for immunomodulatory applications.

Together, the biodistribution results reveal crucial structure–transport relationships in the context of intranasal delivery to the CNS via ZnPc-PGA nanocarriers. While the smaller ZnPc–PGA$_{20}$ undergoes rapid clearance via renal and systemic routes, the larger ZnPc–PGA$_{200}$ and crosslinked ZnPc–PGA$_{200}$–CL exhibit enhanced tissue retention and lymphoid targeting without compromising brain accessibility (Figure 7). These differences underscore the importance of tuning nanocarrier size, stability, and mucoadhesive interactions to balance residence time, clearance, and target tissue accumulation; furthermore, these data position ZnPc–PGA$_{200}$–CL as a particularly promising candidate for intranasal delivery of therapeutics targeting both CNS and immunological targets.

2.5.3 | Comprehensive Safety and Biocompatibility Profile of ZnPc-PGA Nanocarriers

To evaluate the translational potential of ZnPc-PGA nanocarriers following intranasal administration, we carried out comprehensive toxicological assessments, combining in vitro immunocompatibility assays with toxicity analyses. These studies aimed to determine whether structural modifications (e.g., increased polymer arm length or disulfide crosslinking) altered safety profiles under conditions relevant to the clinics.

We first assessed in vitro cytotoxicity using primary peripheral blood mononuclear cells (PBMCs) isolated from three independent healthy donors. A 72 h exposure provided evidence of favorable tolerability for all tested ZnPc-PGA nanocarriers (Figure 8A); ZnPc–PGA$_{20}$ exposure associated with near-complete cell viability (100%), while ZnPc–PGA$_{200}$ and ZnPc–PGA$_{200}$–CL induced modest non-statistically significant reductions in cell viability (~80%). These findings suggest minimal off-target toxicity across different polypeptidic architectures, including those designed for enhanced mucosal retention. To evaluate potential immunotoxicity, we assessed complement activation by quantifying plasma levels of the terminal complement complex SC5b-9 in the same donors. As expected, the positive control (Zymosan) induced a robust complement response; in contrast, ZnPc–PGA$_{20}$, ZnPc–PGA$_{200}$, and ZnPc–PGA$_{200}$–CL did not elicit any measurable increase in SC5b-9 levels relative to the negative control (PBS), indicating that they did not activate complement under the conditions tested (Figure 8B). These results highlight the hemocompatibility of ZnPc-PGA nanocarriers, even in the presence of structural modifications such as crosslinking. We next evaluated the in vivo safety of ZnPc-PGA nanocarriers in healthy Balb/c mice following intranasal administration at a dose of 30 µg ZnPc equivalent per animal. We monitored mice for 48 h post-administration and did not observe significant differences in body weight across groups compared with untreated controls (Figure S22A). Similarly, organ weights (including liver, kidney, spleen, heart, lungs, and brain) remained unchanged, suggesting the absence of acute organ toxicity (Figure S22B–J).

To further investigate systemic responses, we performed biochemical analyses of plasma collected at 24 h post-treatment. We quantified markers of hepatic and renal function – lactate dehydrogenase (LDH), creatinine, aspartate aminotransferase (AST), and alanine aminotransferase (ALT) (Figure 8C–F). We detected no statistically significant changes in LDH or creatinine levels after exposure to ZnPc–PGA$_{20}$, ZnPc–PGA$_{200}$, and ZnPc–PGA$_{200}$–CL, confirming the absence of cellular injury/nephrotoxicity. While AST levels remained stable, we observed a modest but statistically significant decrease in ALT in ZnPc–PGA$_{20}$-treated mice compared with controls (Figure 7F). Importantly, this isolated decrease in ALT activity did not indicate hepatocellular dysfunction (we did not observe an accompanying alteration in AST or LDH levels) and falls within the range of physiological variation reported in prior studies [71].

Taken together, these results establish ZnPc-PGA nanocarriers as biocompatible and well-tolerated. The absence of complement activation, systemic toxicity, or organ-specific adverse effects supports clinical translation; moreover, maintaining the safety profile despite architectural changes (polymer arm length and crosslinking) underscores the versatility of ZnPc-PGA nanocarriers. This evidence of biosafety remains essential to support future development of ZnPc-PGA-based systems for non-invasive brain-targeted therapies.

3 | Conclusions

This study introduces a modular theranostic platform based on ZnPc–initiated NCA-ROP, yielding star-shaped ZnPc-PGA nanocarriers with defined architecture and multifunctionality. Tuning the polypeptide arm length (PGA$_{20}$ versus PGA$_{200}$) controlled solubility, payload capacity, and supramolecular organization, enabling tailored performance across delivery, imaging, and therapy in vitro. Structural and conformational analyses, combining UV–vis spectroscopy, DLS, SAXS, and TEM, revealed that ZnPc-PGA nanocarriers self-assembled into compact cylindrical architectures with architecture-dependent hydration and π–π stacking. SAXS confirmed the formation of cylindrical morphologies and subtle conformational changes upon drug loading or crosslinking, while TEM validated the formation and stability of nanofibers.

ZnPc-PGA nanocarriers displayed efficient cellular uptake, endo-lysosomal sequestration, and long-lived intracellular fluorescence, supporting image-guided delivery. In both 2D and physiologically relevant 3D models (including GBM-on-a-chip

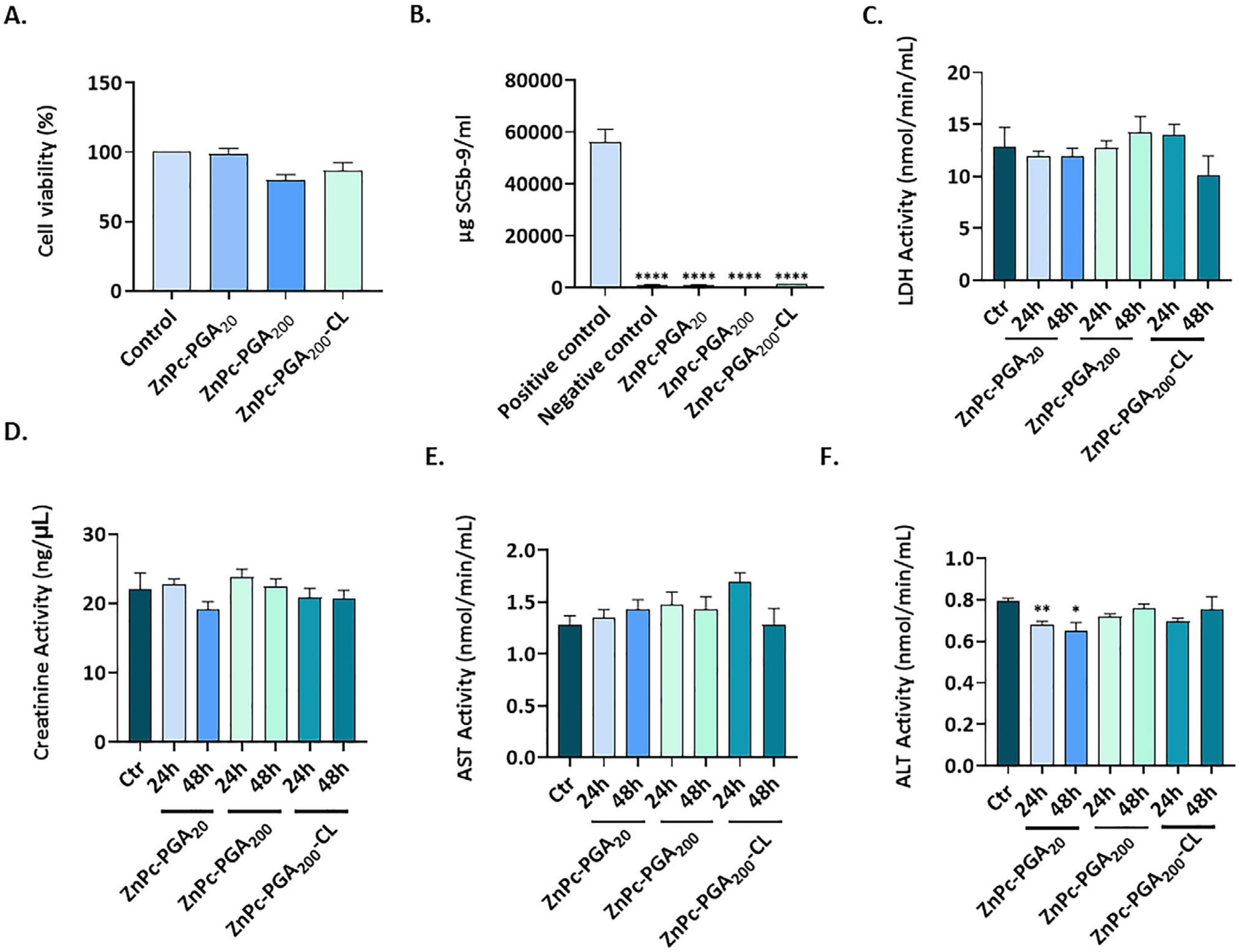

FIGURE 8 | ZnPc-PGA$_{20}$, ZnPc-PGA$_{200}$, and ZnPc-PGA$_{200}$-CL display a robust safety profile. (A) Cytotoxicity assessment of ZnPc-PGA$_{20}$, ZnPc-PGA$_{200}$, and ZnPc-PGA$_{200}$-CL in PBMCs after 72 h of exposure. One-way ANOVA test compared each carrier to the non-treated control; data represented as mean ± SEM from three independent blood donors. (B) Quantification of SC5b-9 complex levels in serum samples of three independent healthy donors after treatment with ZnPc-PGA$_{20}$, ZnPc-PGA$_{200,}$ and ZnPc-PGA$_{200}$-CL. Positive (zymosan) and negative (PBS) controls included for comparison. One-way ANOVA test compared each carrier and negative control to the positive control; data presented as mean ± SEM from three independent donors. Significance reported as ****$p < 0.0001$. (C-F) Analysis of LDH and creatinine levels and AST and ALT activity in blood from Balb/c healthy mice at 24 and 48 h after ZnPc-PGA$_{20}$, ZnPc-PGA$_{200,}$ and ZnPc-PGA$_{200}$-CL administration. One-way ANOVA test compared each carrier to the non-treated control; data represented as mean ± SEM of at least three animals. Significance reported as *$p < 0.05$, **$p < 0.01$). One-way ANOVA test compared normalized fluorescence intensity (FI) in arbitrary units (a.u.) between ZnPc-PGA$_{20}$ and ZnPc-PGA$_{200}$ for each time point; $n = 3$, mean ± SEM. Significance reported as *$p \leq 0.05$, ns = non-significant.

microfluidic systems), ZnPc-PGA nanocarriers demonstrated deep penetration and architecture-dependent PDT efficacy. Notably, ZnPc–PGA$_{20}$ diffused rapidly and uniformly in dense tumor-like matrices, while ZnPc–PGA$_{200}$, with slower kinetics, offered enhanced solubility and conjugation potential. Hypoxia-tunable microfluidic studies revealed that oxygen availability, rather than delivery, limited therapeutic efficacy, highlighting the value of ZnPc-PGA nanocarriers for mechanistic dissection of PDT resistance in solid tumors.

To expand the therapeutic scope, we leveraged the pendant carboxyl groups of PGA$_{200}$ for the covalent conjugation of PTX, yielding ZnPc–PGA$_{200}$–PTX. Spectroscopic and SAXS analyses revealed altered chromophore packing and increased flexibility at the periphery, consistent with reduced self-quenching and enhanced dispersion of the therapeutic payload. ZnPc–PGA$_{200}$–PTX displayed synergistic cytotoxicity under irradiation, combining PDT and chemotherapy in a single covalently integrated agent.

To translate these materials toward CNS applications, we developed a crosslinked formulation (ZnPc–PGA$_{200}$–CL) optimized for intranasal administration via formulation in a hydrogel delivery system. Leveraging intrinsic ZnPc fluorescence as a stable imaging reporter, we tracked biodistribution in vivo and observed significant accumulation in the brain, olfactory bulbs, and mucosa thanks to enhanced nose-to-brain delivery. Crosslinking enhances retention in lymphoid tissues, such as the spleen, further broadening the potential applications in immunomodulation. Notably, all nanocarriers, regardless of architecture or formulation, exhibited favorable toxicological profiles, with no systemic toxicity or complement activation in vitro or in vivo.

Proteomic characterization of the protein corona revealed the consistent enrichment of fibrinogen chains, cytoskeletal components, and olfactory-associated proteins for both ZnPc–PGA_{20} and ZnPc–PGA_{200}. Functional annotation of these proteins indicated associations with biological processes that included coagulation, immune regulation, intracellular trafficking, and olfactory signaling. These compositional features suggest potential roles for the nano–bio interface in modulating interactions with biological systems, including processes such as adhesion, transport, and immune recognition. Reactome pathway enrichment analysis further supported these associations. While these findings do not establish direct functional outcomes, they provide insight into how corona composition may contribute to the biological identity of the nanoplatform and influence interactions within complex environments. These observations are consistent with the concept of the "protein-nanoparticle interface" and underscore the importance of considering corona-mediated effects in the design of multifunctional polymer systems.

Despite the promising multifunctionality of the ZnPc-PGA platform, we acknowledge several translational challenges. PDT for tumors located deep within the brain remains limited by light penetration, requiring minimally invasive stereotactic interstitial irradiation strategies for clinical implementation. Moreover, although our data demonstrate sustained brain retention and structurally dependent distribution patterns, achieving therapeutically optimal and spatially homogeneous intratumoral drug levels remains a critical objective of ongoing investigations. Furthermore, the field lacks standardized benchmark nanocarriers for intranasal brain targeting, as reported systems are highly formulation-specific and evaluated under heterogeneous experimental conditions, limiting direct cross-platform comparison.

In this context, our findings position ZnPc-PGA nanocarriers as a multifunctional, well-characterized class of star-shaped polypeptide with intrinsic optical properties. The tunable architecture and comprehensive physicochemical and biointerface-interaction characterization underscore the role of molecular design in governing supramolecular organization and functional responses in complex environments. Their ability to reach the brain via intranasal administration, favorable safety profile, and multifunctionality provide a basis for future in vivo validation in challenging tumor models such as GBM.

4 | Experimental Section

4.1 | Materials

All chemicals were reagent grade, purchased from Sigma–Aldrich, and used without further purification, unless otherwise indicated. H-L-Glu(OBzl)-OH and H-L-Glu(OtBu)-OH were purchased from Iris Biotech. Zinc (II) 2,9,16,23-tetra(amino)phthalocyanine was purchased from Porphychem. Acetone, TFA, and HBr solution (48 wt.%) in water were purchased from Acros. Diethyl ether was purchased from Sharlab. Anhydrous N,N-DMF and DMSO, and LC-MS-grade acetonitrile and methanol were purchased from Fisher Scientific. 2-mercaptoethanol was purchased from Merck. Polyethylene oxide standards were purchased from Tosoh (Japan). Ultrapure water with a resistivity of 18 MΩ·cm was used for all aqueous preparations. All deuterated samples were purchased from Deutero GmbH. Dialysis was performed using a Millipore ultrafiltration device fitted with a 3 kDa molecular weight cut-off (MWCO) regenerated cellulose membrane 20 (Vivaspin). U251MG cells were purchased from Sigma–Aldrich (09063001), and the A172 GBM cell line was kindly provided by Dr. Julia Lorenzo (Universitat Autònoma de Barcelona, UAB). Dulbecco's Modified Eagle's Medium (DMEM) with high glucose was purchased from Sigma. DCFH was purchased from MedChemExpress. PBS, FBS, penicillin and streptomycin (P/S), and trypsin were purchased from Gibco Life Technologies. MTS/PMS assays were supplied by Promega.

4.2 | ZnPc-PGA_{20} and ZnPc-PGA_{200} Synthesis and Characterization

Protected Glu-NCA monomers (OtBu or OBzl) were polymerized via ROP in anhydrous DMF or DMSO using Zn(II) tetra(amino)phthalocyanine as a macroinitiator at defined $[MM]_0/[I]_0$ ratios. Reactions were conducted at -4°C (120 h) or at room-temperature (72 h) and monitored by IR for the disappearance of NCA carbonyl bands. Crude polymers were precipitated in diethyl ether, isolated by centrifugation, and dried under vacuum, yielding 70%–90% of protected ZnPc-PGA. Protecting groups were removed under acidic conditions using HBr in water. Deprotected polymers were neutralized with $NaHCO_3$ and purified by dialysis (3 kDa MWCO) to obtain water-soluble ZnPc-PGA nanocarriers, which were characterized by ^{1}H-NMR, UV–vis, SEC-MALS-RI-Viscometer, DLS, CD, TEM, scanning electron microscopy, Cryo-TEM, and SAXS.

4.3 | ZnPc-PGA_{200}-PTX Synthesis and Characterization

ZnPc-PGA_{200} (acid form) was activated in anhydrous DMF in a nitrogen environment using diisopropylcarbodiimide (DIC)/1-hydroxy-benzotriazole (HOBt) and subsequently reacted with PTX in the presence of catalytic 4-dimethylaminopyridine (DMAP) at pH 8. After 24 h, ZnPc-PGA_{200}-PTX was precipitated in cold ether, washed, neutralized with $NaHCO_3$, desalted by ultrafiltration (3 kDa MWCO), and lyophilized to afford ZnPc-PGA_{200}-PTX as a green powder at a 95% yield. Conjugation was confirmed by ^{1}H-NMR in D_2O. ZnPc-PGA_{200}-PTX was characterized by ^{1}H-NMR, UV–vis, DLS, CD, and SAXS. Free-drug content was analyzed by LC-MS/MS. PTX was extracted from the conjugate using methanol, clarified by centrifugation, and analyzed by LC-MS/MS on a biphenyl column using positive-ion multiple reaction monitoring (MRM) (m/z 855.4 → 286.1). Quantification employed a water/acetonitrile gradient with formic acid. For release kinetics studies, ZnPc-PGA_{200}-PTX was incubated at 37°C in pH 7.4 (DPBS) or pH 5 (acetate buffer). Aliquots collected over 72 h were lyophilized, extracted with methanol, and analyzed by LC-MS/MS.

4.4 | ZnPc-PGA$_{200}$-CL Synthesis and Characterization

ZnPc-PGA was functionalized with PD at 10 mol.% via the activation of glutamic acid with 4-(4,6-dimethoxy-1,3,5-triazin-2-yl)-4-methylmorpholinium tetrafluoroborate (DMTMM BF4) in anhydrous DMF, followed by the addition of PD cysteamine at pH 8. After 48 h at room-temperature, ZnPc-PGA$_{200}$-PD was precipitated in ether, neutralized with $NaHCO_3$, and purified by dialysis (3 kDa MWCO). PD loading was quantified by ^{1}H-NMR, yielding ~70% isolated product with ~80% conjugation efficiency. ZnPc-PGA$_{200}$-CL was synthesized by mixing aqueous solutions of ZnPc-PGA$_{200}$-PD (8% PD) and hexa(ethylene glycol) dithiol at 4°C, followed by immediate precipitation in cold acetone to induce crosslinking. After 4 h at room-temperature, the reaction was quenched with β-mercaptoethanol, acetone was removed, and the product was dialyzed (3 kDa MWCO) and lyophilized to yield a green powder.

4.5 | Protein Corona Analysis

Protein corona formation was assessed by incubating nanoparticles with undiluted human serum or FBS for 1 h, followed by a series of five centrifugation and washing steps to separate soft and hard corona fractions. Pellets and supernatants were collected, and total protein content was quantified prior to LC-MS/MS preparation. Samples were processed using the in-StageTip method, including thermal lysis, reduction/alkylation, enzymatic digestion with trypsin/LysC, and peptide purification on C18 filters. Eluted peptides were dried, reconstituted to 1 µg µL^{-1}, and analyzed (200 ng per sample) using an Evosep One LC system coupled to a timsTOF Pro 2 operated in DIA-PASEF mode (a data-independent acquisition [DIA] method that uses parallel accumulation-serial fragmentation [PASEF] technology). Protein identification and label-free quantification were performed using PaSER and DIA-NN software against a human reference library, yielding label-free quantification values for all corona-associated proteins.

4.6 | Cell Culture Protocols

U251MG and A172 GBM cells were cultured in DMEM high glucose medium supplemented with 10% FBS and 1% P/S. Cells were maintained at 37°C in a 5% CO_2 atmosphere. The cell media was replaced every 2–3 days, and cells were passaged when they reached 80% confluence (once weekly).

4.7 | Live-Cell Imaging

A172 and U251MG cells were seeded in 384-well imaging plates and incubated for 24 h prior to treatment with ZnPc-PGA$_{20}$ or ZnPc-PGA$_{200}$ at 5.4 µM ZnPc equivalent doses. MitoTracker Green (mitochondria, 0.1 µM) and LysoTracker Blue (lysosomes, 1 µM) were added 1 h before imaging. Live-cell uptake was monitored using a Leica TCS SP8 confocal microscope with 405/561/638 nm excitation, under controlled temperature and CO_2 conditions. Images were processed using LAS X software.

4.8 | Cellular Uptake Studies by Flow Cytometry

Cells were seeded in 12-well plates and incubated with 2.2 µM equivalents of ZnPc-PGA$_{20}$ or ZnPc-PGA$_{200}$ at different time points. Uptake was evaluated at 37°C and 4°C to distinguish active versus passive internalization. After incubation, cells were washed, trypsinized, stained with PI, and analyzed by flow cytometry (CytoFLEX S, 635 nm excitation, 750 nm emission). Autofluorescence was subtracted, and data were reported as CAF (RFU) normalized by cell viability. Three independent biological replicates ($n = 3$) were performed.

4.9 | Cell Viability After PDT with MTS Assay

A172 and U251MG cells were seeded in sterile 96-well plates and allowed to adhere for 24 h at 37°C and 5% CO_2. Then, ZnPc-PGA nanocarriers were incubated for 48 h, followed by irradiation at light doses of 0–70 J cm^{-2} using a Lumidox II LED array ($\lambda \geq$ 606 nm). Viability was measured 24 h later via MTS/PMS assay and normalized to irradiated controls. Experiments included three biological replicates, each with three technical replicates.

4.10 | Reactive Oxygen Species Production

A172 cells were incubated with ZnPc-PGA$_{20}$ and ZnPc-PGA$_{200}$ for 48 h and irradiated (70 J cm^{-2}). At defined time points, cells were harvested, incubated with DCFH to quantify intracellular ROS and PI to assess viability, and analyzed by flow cytometry (10 000 events/sample). Data were normalized to matched irradiated or untreated controls across three biological replicates.

4.11 | Exosome Detection After PDT

Exosome presence following sub-IC$_{50}$ PDT doses was quantified using an AlphaLISA bead-based assay targeting CD9 and CD63. Cell supernatants were incubated with CD9 acceptor beads and biotinylated CD63 antibodies, followed by streptavidin donor beads. Upon 680 nm excitation, donor–acceptor proximity generated a 615 nm emission signal proportional to exosome abundance. Signals were normalized to cell viability.

4.12 | 3D Cultures and Organ-on-a-Chip Model

Type I collagen hydrogels (2 mg mL^{-1}) were prepared by mixing rat-tail collagen with NaOH, PBS, and sterile water, then combined 1:1 (v/v) with cell suspensions before seeding into 96-well plates and Be-Gradient microfluidic devices. Gels were polymerized at 37°C and overlaid with culture medium overnight prior to polymer incubation. The microfluidic device features a central 3D collagen chamber flanked by perfusion channels, enabling nutrient diffusion and the formation of oxygen gradients due to the gas-impermeable cyclic olefin polymer material. Normoxic and hypoxic conditions were established using concentrations of 10^6 and 10^7 cells·mL^{-1}, respectively, with devices maintained on a rocker to simulate flow. Hypoxia within the device was monitored using ImageIT Red, which fluoresces at low O_2 levels (< 5%). PDT efficacy in 3D cultures was assessed using the PrestoBlue viability assay, with fluorescence measured after 2–3 h incubation. Live/dead staining used calcein-AM to stain viable cells. Confocal imaging was performed on a STELLARIS DLS microscope, and FI profiles across the 3D chamber were quantified using Fiji software.

4.13 | Animal Studies

Animal experiments were conducted in accordance with European Communities Council Directive 86/609/ECC and Spanish Royal Decree 1201/2005, with approval from the Institutional Animal Care and Use Committee (Ref: 2025-VSC-PEA-0132). Male and female Balb/c mice (6–8 weeks old) were obtained from Inotiv and housed in the animal facility at the Prince Felipe Research Center (CIPF, València, Spain). Animals were housed under specific-pathogen-free conditions with controlled temperature (22 ± 2°C), humidity (50%–60%), and a 12-h light-dark cycle. Food and water were provided ad libitum, and environmental enrichment was included. Mice were euthanized using CO_2 inhalation following ethical protocols.

4.14 | Statistical Analysis

Data presented as mean ± standard error of the mean (SEM). No outliers were excluded. Statistical analyses were performed using GraphPad Prism 9 (GraphPad Software, USA). Differences were considered statistically significant when $p < 0.05$. Drug interaction effects were evaluated using the Bliss independence model, where Bliss score values of < 0 indicate antagonism, 0-to-0 indicate additivity (lack of synergism/antagonism), and > 0 indicate synergism.

Author Contributions

A.B.-F. led the synthesis of the nanocarriers and the derivatives, conformational studies, data curation, formal analysis, investigation, methodology, and writing of the original draft. Cell viability assays and biological studies in 2D cell cultures were carried out by A.B.-F. with support from E.M.S. Cell viability assays and biological studies in 3D cell cultures, including Organ-on-a-chip, were carried out by T.R., C.B., and A.B.-F. under the supervision of I.O. Animal studies, including biodistribution and toxicology profile, were led by A.A. and P.C.-M. TEM and Cryo-TEM analysis were led by V.S. Protein corona studies were led by M.S.-F. and P.J.-V. C.H.-I. led the SAXS analysis. S.D. led SEC-MALS-Viscometer-RI characterization. M.M., I.C-S, and M.J.V. cosupervised the study and contributed to data curation and formal analysis, as well as to the writing process. Conceptualization was led by M.J.V., with support from M.M. and I.C-S. M.J.V. led funding acquisition and project administration. The manuscript was written by A.B.-F. and M.J.V., with contributions from all authors in reviewing and editing. All authors have read and approved the final version of the manuscript.

Acknowledgements

Nanocarrier biodistribution images were acquired in the Biomedical Imaging and Metabolomics Section of the Central Unit for Medical Research (UCIM) at the University of València. T.R., C.B., and I.O. also acknowledge the use of Servicio General de Apoyo a la Investigación-SAI, Universidad de Zaragoza, and the collaboration of the Unidad de Apoyo Preclínico de Aragón (UAPA) at the Aragón Health Research Institute (IISA). The authors thank Dr. Stuart P. Atkinson for his help with manuscript development and English editing, and Alicia Martinez Romero for flow cytometry analysis. The authors would also like to thank Prof. Beatriu Escuder and Martina La Manna from UJI for facilitating the scanning electron microscopy analysis. The authors would like to acknowledge Pablo Sánchez Cano for the support with synthesis.

Funding

Association for Cancer Research (AECC) for the Ph.D. grant to ABF (Ref PRDVA222470BENA) and AECC Junior Grant (Ref INVES211323CONE) to ICS. Spanish Ministry of Science, Innovation and Universities (PID2023-152459OB-I00) funded by MICIU/AEI/10.13039/501100011033. This study forms part of the Advanced Materials program and was supported by MCIN with funding from the European Union NextGenerationEU (PRTR-C17.I1) Acronym Pol@Mets. Ref. MFA/2022/065). Funding support from CIBERONC (CB22/12/0048) is also acknowledged. SAXS measurements were acquired at the NCD-SWEET beamline at the ALBA Synchrotron Light source in Barcelona, Spain, through Project ID 2024098803 led by M.M., T.R., C.B., and I.O., acknowledged support from the Spanish Ministry of Economy and Competitiveness (MINECO fellowship, DIN 2020–011544); Ministry of Science and Innovation, the Agency, and the European Regional Development Fund (PID2021-126051OB-C41 funded by MCIN /AEI /10.13039/501100011033 / FEDER, UE) and by the Gobierno de Aragón and Fondo Social Europeo (T62_23R).

Conflicts of Interest

The authors declare no conflicts of interest.

Data Availability Statement

The data that support the findings of this study are available from the corresponding author upon reasonable request.

References

1. J. Tang, N. Karbhari, and J. L. Campian, “Therapeutic Targets in Glioblastoma: Molecular Pathways, Emerging Strategies, and Future Directions,” *Cells* 14 (2025): 494, https://doi.org/10.3390/cells14070494.

2. A. Pouyan, M. Ghorbanlo, M. Eslami, et al., “Glioblastoma Multiforme: Insights into Pathogenesis, Key Signaling Pathways, and Therapeutic Strategies,” *Molecular Cancer* 24 (2025): 58.

3. S. S. K. Yalamarty, N. Filipczak, X. Li, et al., “Mechanisms of Resistance and Current Treatment Options for Glioblastoma Multiforme (gbm), *Cancers (Basel)*,” *Cancers* 15 (2023): 2116, https://doi.org/10.3390/cancers15072116.

4. C. Saraiva, C. Praça, R. Ferreira, T. Santos, L. Ferreira, and L. Bernardino, “Nanoparticle-Mediated Brain Drug Delivery: Overcoming Blood–Brain Barrier to Treat Neurodegenerative Diseases,” *Journal of Controlled Release* 235 (2016): 34–47, https://doi.org/10.1016/j.jconrel.2016.05.044.

5. F. Ahmad, R. Varghese, S. Panda, et al., “Smart Nanoformulations for Brain Cancer Theranostics: Challenges and Promises,” *Cancers* 14 (2022): 5389, https://doi.org/10.3390/cancers14215389.

6. W. Tang, W. Fan, J. Lau, L. Deng, Z. Shen, and X. Chen, “Emerging Blood–Brain-Barrier-Crossing Nanotechnology for Brain Cancer Theranostics,” *Chemical Society Reviews* 48 (2019): 2967–3014, https://doi.org/10.1039/C8CS00805A.

7. H. Azimizonuzi, A. Ghayourvahdat, M. H. Ahmed, et al., “A state-of-the-Art Review of the Recent Advances of Theranostic Liposome Hybrid Nanoparticles in Cancer Treatment and Diagnosis,” *Cancer cell international* 25 (2025): 26, https://doi.org/10.1186/s12935-024-03610-z.

8. H.-J. Liu and P. Xu, “Strategies to Overcome/Penetrate the BBB for Systemic Nanoparticle Delivery to the Brain/Brain Tumor,” *Advanced Drug Delivery Reviews* 191 (2022): 114619, https://doi.org/10.1016/j.addr.2022.114619.

9. D. Liu, X. Dai, Z. Tao, et al., “Advances in Blood–Brain Barrier-Crossing Nanomedicine for Anti-glioma,” *Cancer Nanotechnology* 14 (2023): 58, https://doi.org/10.1186/s12645-023-00211-9.

10. Y. Jia, Y. Wu, F. Zhang, Y. Sun, and Y. Liu, “Anotechnology-Enhanced photodynamic Therapy for Glioblastoma Treatment,” *Chemical Communications* 61 (2025): 12431–12448, https://doi.org/10.1039/D5CC03192C.

11. A. Benaicha-Fernández, S. P. Atkinson, I. Conejos-Sánchez, M. Medel, and M. J. Vicent, “Polymer-Based Nanomedicines: Supporting Multimodal Approaches to Glioblastoma Multiforme Treatment,” *Advanced Drug Delivery Reviews* 228 (2026): 115735, https://doi.org/10.1016/j.addr.2025.115735.

12. W. Stummer, U. Pichlmeier, T. Meinel, O. D. Wiestler, F. Zanella, and H.-J. Reulen, “Fluorescence-Guided Surgery with 5-Aminolevulinic Acid for Resection of Malignant Glioma: A Randomised Controlled Multicentre Phase III trial,” *The Lancet Oncology* 7 (2006): 392–401, https://doi.org/10.1016/S1470-2045(06)70665-9.

13. C. Cao, Z. Jin, X. Shi, et al., “First Clinical Investigation of near-infrared Window Iia/Iib Fluorescence Imaging for Precise Surgical Resection of Gliomas,” *IEEE Transactions on Biomedical Engineering* 69 (2022): 2404–2413, https://doi.org/10.1109/TBME.2022.3143859.

14. D. Reichel, B. Sagong, J. Teh, et al., “Near Infrared Fluorescent Nanoplatform for Targeted Intraoperative Resection and Chemotherapeutic Treatment of Glioblastoma,” *ACS Nano* 14 (2020): 8392–8408, https://doi.org/10.1021/acsnano.0c02509.

15. A. L. Vahrmeijer, M. Hutteman, J. R. Van Der Vorst, C. J. H. Van De Velde, and J. V. Frangioni, “Image-Guided Cancer Surgery Using Near-Infrared Fluorescence,” *Nature Reviews Clinical Oncology* 10 (2013): 507–518, https://doi.org/10.1038/nrclinonc.2013.123.

16. S. Mallidi, S. Anbil, A.-L. Bulin, G. Obaid, M. Ichikawa, and T. Hasan, “Beyond the Barriers of Light Penetration: Strategies, Perspectives and Possibilities for Photodynamic Therapy,” *Theranostics* 6 (2016): 2458–2487, https://doi.org/10.7150/thno.16183.

17. R. C. H. Wong, P. C. Lo, and D. K. P. Ng, “Stimuli Responsive Phthalocyanine-based Fluorescent Probes and Photosensitizers,” *Coordination Chemistry Reviews* 379 (2019): 30–46, https://doi.org/10.1016/j.ccr.2017.10.006.

18. S. Liu, J. Ma, E. Y. Xue, et al., “Polymeric Phthalocyanine-Based Nanosensitizers for Enhanced Photodynamic and Sonodynamic Therapies,” *Advanced healthcare materials* 12 (2023): 2300481, https://doi.org/10.1002/adhm.202300481.

19. E. Ahmetali, P. Sen, N. C. Süer, T. Nyokong, T. Eren, and M. K. Şener, “Photodynamic Therapy Activities of Phthalocyanine-Based Macromolecular Photosensitizers on Mcf-7 Breast Cancer Cells,” *Journal of Macromolecular Science, Part A* 58 (2021): 748–757, https://doi.org/10.1080/10601325.2021.1934012.

20. T. Potlog, A. Popusoi, I. Lungu, S. Robu, and I. Bulimestru, “Photophysics of Tetracarboxy-Zinc Phthalocyanine Photosensitizers,” *RSC Advances* 12 (2022): 31778–31785, https://doi.org/10.1039/D2RA05676C.

21. I. Drath, F. Richter, and M. Feja, “Nose-to-brain Drug Delivery: From Bench to Bedside,” *Translational Neurodegeneration* 14 (2025): 23, https://doi.org/10.1186/s40035-025-00481-w.

22. Y. Qiu, S. Huang, L. Peng, et al., “The Nasal–Brain Drug Delivery Route: Mechanisms and Applications to Central Nervous System Diseases,” *MedComm* 6 (2025): 70213, https://doi.org/10.1002/mco2.70213.

23. W. K. Paraiso, C. Palacín Ramos, P. M. Hossain, et al., “Overcoming Barriers: Nanomedicine-Based Strategies for Nose-to-Brain Delivery,” *Nanoscale* 18 (2026): 66–89, https://doi.org/10.1039/D5NR02259B.

24. V. Deshmukh, N. S. Pathan, N. Haldar, et al., “Exploring Intranasal Drug Delivery via Nanocarriers: A Promising Glioblastoma Therapy,” *Colloids and Surfaces B: Biointerfaces* 245 (2025): 114285, https://doi.org/10.1016/j.colsurfb.2024.114285.

25. A. Duro-Castano, R. M. England, D. Razola, et al., “Well-Defined Star-Shaped Polyglutamates With Improved Pharmacokinetic Profiles as Excellent Candidates for Biomedical Applications,” *Molecular Pharmaceutics* 12 (2015): 3639–3649, https://doi.org/10.1021/acs.molpharmaceut.5b00358.

26. T. Ikeuchi, J. Mack, T. Nyokong, N. Kobayashi, and M. Kimura, “Aggregation Control of Robust Water-Soluble Zinc(ii) Phthalocyanine-Based Photosensitizers,” *Langmuir* 32 (2016): 11980–11985, https://doi.org/10.1021/acs.langmuir.6b03552.

27. X. Li, K. Jeong, Y. Lee, et al., “Water-Soluble Phthalocyanines Selectively Bind to Albumin Dimers: A Green Approach Toward Enhancing Tumor-Targeted Photodynamic Therapy,” *Theranostics* 9 (2019): 6412–6423, https://doi.org/10.7150/thno.35210.

28. F. Lv, B. Cao, Y. Cui, and T. Liu, “Zinc Phthalocyanine Labelled Polyethylene Glycol: Preparation, Characterization, Interaction With Bovine Serum Albumin and near Infrared Fluorescence Imaging in Vivo,” *Molecules* 17 (2012): 6348–6361, https://doi.org/10.3390/molecules17066348.

29. M. J. Hajipour, R. Safavi-Sohi, S. Sharifi, et al., “An Overview of Nanoparticle Protein Corona Literature,” *Small* 19 (2023): 2301838, https://doi.org/10.1002/smll.202301838.

30. H. Li, Y. Wang, Q. Tang, et al., “The Protein Corona and Its Effects on Nanoparticle-based Drug Delivery Systems,” *Acta Biomaterialia* 129 (2021): 57–72, https://doi.org/10.1016/j.actbio.2021.05.019.

31. N. Bertrand, P. Grenier, M. Mahmoudi, et al., “Mechanistic Understanding of in Vivo Protein Corona Formation on Polymeric Nanoparticles and Impact on Pharmacokinetics,” *Nature Communications* 8 (2017): 777, https://doi.org/10.1038/s41467-017-00600-w.

32. S. Behzadi, V. Serpooshan, R. Sakhtianchi, et al., “Protein Corona Change the Drug Release Profile of Nanocarriers: The “Overlooked” Factor at the Nanobio Interface,” *Colloids Surfaces B Biointerfaces* 123 (2014): 143–149.

33. L. Zhang, B. Casey, D. K. Galanakis, et al., “The Influence of Surface Chemistry on Adsorbed Fibrinogen Conformation, Orientation, Fiber Formation and Platelet Adhesion,” *Acta Biomaterialia* 54 (2017): 164–174, https://doi.org/10.1016/j.actbio.2017.03.002.

34. E. Dejana, M. Lampugnani, M. Giorgi, M. Gaboli, and P. Marchisio, “Fibrinogen Induces Endothelial Cell Adhesion and Spreading via the Release of Endogenous Matrix Proteins and the Recruitment of More Than One Integrin Receptor,” *Blood* 75 (1990): 1509–1517, https://doi.org/10.1182/blood.V75.7.1509.1509.

35. M. Qiu, Y. Tang, J. Chen, et al., “Lung-selective Mrna Delivery of Synthetic Lipid Nanoparticles for the Treatment of Pulmonary Lymphangioleiomyomatosis,” *Proceedings of the National Academy of Sciences* 119 (2022): 2116271119, https://doi.org/10.1073/pnas.2116271119.

36. C. Fedeli, D. Segat, R. Tavano, et al., “The Functional Dissection of the Plasma Corona of Sio $_2$ -nps Spots Histidine Rich Glycoprotein as a Major Player Able to Hamper Nanoparticle Capture by Macrophages,” *Nanoscale* 7 (2015): 17710–17728, https://doi.org/10.1039/C5NR05290D.

37. C. Marques, M. J. Hajipour, C. Marets, et al., “Identification of the Proteins Determining the Blood Circulation Time of Nanoparticles,” *ACS Nano* 17 (2023): 12458–12470, https://doi.org/10.1021/acsnano.3c02041.

38. J. Meinhardt, J. Radke, C. Dittmayer, et al., “Olfactory Transmucosal sars-cov-2 Invasion as a Port of Central Nervous System Entry in Individuals with Covid-19,” *Nature Neuroscience* 24 (2020): 168–175.

39. M. P. Monopoli, C. Åberg, A. Salvati, and K. A. Dawson, “Biomolecular Coronas Provide the Biological Identity of Nanosized Materials,” *Nature Nanotechnology* 7 (2012): 779–786, https://doi.org/10.1038/nnano.2012.207.

40. F. N. Velazquez, M. Miretti, M. T. Baumgartner, B. L. Caputto, T. C. Tempesti, and C. G. Prucca, “Effectiveness of ZnPc and of an Amine Derivative to Inactivate Glioblastoma Cells by Photodynamic THERAPY: An In Vitro Comparative Study,” *Scientific Reports* 9 (2019): 3010, https://doi.org/10.1038/s41598-019-39390-0.

41. J. Li, G. Wang, Y. Mai, et al., “Lysosome-localization and Tumor-Targeting of Novel Photosensitizers Enhance the Ablation of Cancer,” *Journal of Photochemistry and Photobiology B: Biology* 261 (2024): 113045, https://doi.org/10.1016/j.jphotobiol.2024.113045.

42. K. Aubertin, A. K. A. Silva, N. Luciani, et al., “Massive Release of Extracellular Vesicles From Cancer Cells After Photodynamic Treatment or Chemotherapy,” *Scientific Reports* 6 (2016): 35376, https://doi.org/10.1038/srep35376.

43. B. Mkhobongo, R. Chandran, and H. Abrahamse, “The Role of Melanoma Cell-Derived Exosomes (mtex) and Photodynamic Therapy (pdt) Within a Tumor Microenvironment,” *International Journal of Molecular Sciences* 22 (2021): 9726, https://doi.org/10.3390/ijms22189726.

44. M. Czystowska-Kuzmicz and T. L. Whiteside, “The Potential Role of Tumor-Derived Exosomes in Diagnosis, Prognosis, and Response to Therapy in Cancer,” *Expert Opinion on Biological Therapy* 21 (2020): 241–258, https://doi.org/10.1080/14712598.2020.1813276.

45. Z. Zhao, H. Y. Zhang, Q. Zeng, et al., “Exosomes From 5-aminolevulinic Acid Photodynamic Therapy-Treated Squamous Carcinoma Cells Promote Dendritic Cell Maturation,” *Photodiagnosis and Photodynamic Therapy* 30 (2020): 101746, https://doi.org/10.1016/j.pdpdt.2020.101746.

46. Z. Andreu, E. Masiá, D. Charbonnier, and M. J. Vicent, “A Rapid, Convergent Approach to the Identification of Exosome Inhibitors in Breast Cancer Models,” *Nanotheranostics* 7 (2023): 1–21, https://doi.org/10.7150/ntno.73606.

47. L. E. Ibarra, M. L. Vilchez, M. D. Caverzán, and L. N. Milla Sanabria, “Understanding the Glioblastoma Tumor Biology to Optimize Photodynamic Therapy: From Molecular to Cellular Events,” *Journal of Neuroscience Research* 99 (2021): 1024–1047, https://doi.org/10.1002/jnr.24776.

48. L. Feldman, “Hypoxia Within the Glioblastoma Tumor Microenvironment: A Master Saboteur of Novel Treatments,” *Frontiers in Immunology* 15 (2024): 1384249, https://doi.org/10.3389/fimmu.2024.1384249.

49. A. L. Chédeville, A. Lourdusamy, A. R. Monteiro, R. Hill, and P. A. Madureira, “Investigating Glioblastoma Response to Hypoxia,” *Biomedicines* 8 (2020): 310, https://doi.org/10.3390/biomedicines8090310.

50. B. Pucelik, A. Sułek, A. Barzowska, and J. M. Dąbrowski, “Recent Advances in Strategies for Overcoming Hypoxia in Photodynamic Therapy of Cancer,” *Cancer Letters* 492 (2020): 116–135, https://doi.org/10.1016/j.canlet.2020.07.007.

51. G. Dabkevičiūtė and V. Petrikaitė, “Insights Into 2d and 3d Cell Culture Models for Nanoparticle-Based Drug Delivery to Glioblastoma,” *Biochemical Pharmacology* 237 (2025): 116931.

52. C. Bayona, L. Alza, T. Ranđelović, et al., “Tetralol Derivative NNC-55-0396 Targets Hypoxic Cells in the Glioblastoma Microenvironment: An Organ-On-Chip Approach,” *Cell Death & Disease* 15 (2024): 127, https://doi.org/10.1038/s41419-024-06492-1.

53. J. M. Ayuso, M. Virumbrales-Muñoz, A. Lacueva, et al., “Development and Characterization of a Microfluidic Model of the Tumour Microenvironment,” *Scientific Reports* 6 (2016): 36086, https://doi.org/10.1038/srep36086.

54. S. S. Burić, A. Podolski-Renić, J. Dinić, et al., “Modulation of Antioxidant Potential With Coenzyme q10 Suppressed Invasion of Temozolomide-resistant Rat Glioma in Vitro and in Vivo,” *Oxidative Medicine and Cellular Longevi* 2019 (2019): 3061607.

55. A. Eldar-Boock, R. Blau, C. Ryppa, et al., “Integrin-Targeted Nano-Sized Polymeric Systems for Paclitaxel Conjugation: A Comparative Study,” *Journal of Drug Targeting* 25 (2017): 829–844, https://doi.org/10.1080/1061186X.2017.1358727.

56. Y. Fernández, J. Movellan, L. Foradada, et al., “In Vivo Antitumor and Antimetastatic Efficacy of a Polyacetal-Based Paclitaxel Conjugate for Prostate Cancer Therapy,” *Advanced Healthcare Material* 11 (2022): 2101544, https://doi.org/10.1002/ADHM.202101544.

57. A. Lepland, A. Malfanti, U. Haljasorg, et al., “Depletion of Mannose Receptor–Positive Tumor-Associated Macrophages via a Peptide-Targeted Star-shaped Polyglutamate Inhibits Breast Cancer Progression in Mice,” *Cancer Research Communications* 2 (2022): 533–551, https://doi.org/10.1158/2767-9764.CRC-22-0043.

58. I. Dolz-Pérez, M. A. Sallam, E. Masiá, et al., “Polypeptide-Corticosteroid Conjugates as a Topical Treatment Approach to Psoriasis,” *Journal of Controlled Release* 318 (2020): 210–222, https://doi.org/10.1016/j.jconrel.2019.12.016.

59. P. Thapa, M. Li, M. Bio, et al., “Far-Red Light-Activatable Prodrug of Paclitaxel for the Combined Effects of Photodynamic Therapy and Site-Specific Paclitaxel Chemotherapy,” *Journal of Medicinal Chemistry* 59 (2016): 3204–3214, https://doi.org/10.1021/acs.jmedchem.5b01971.

60. X. Yi, J. Dai, Y. Han, et al., “A High Therapeutic Efficacy of Polymeric Prodrug Nano-assembly for a Combination of Photodynamic Therapy and Chemotherapy,” *Communications Biology* 1 (2018): 202, https://doi.org/10.1038/s42003-018-0204-6.

61. M. Ishizuka, M. Kaibori, F. Sumiyama, et al., “Photodynamic Therapy With Paclitaxel-Encapsulated Indocyanine Green-Modified Liposomes for Breast Cancer,” *Frontiers in Oncology* 14 (2024): 1365305, https://doi.org/10.3389/fonc.2024.1365305.

62. Q. Liu, X. Yin, L. R. Languino, and D. C. Altieri, “Evaluation of Drug Combination Effect Using a Bliss Independence Dose–Response Surface Model,” *Statistics in Biopharmaceutical Research* 10 (2018): 112–122, https://doi.org/10.1080/19466315.2018.1437071.

63. I. Conejos-Sánchez, T. Melnyk, E. Masiá, et al., “A rationally Designed Polypeptide-Based Hybrid Platform for Targeted Intranasal Brain Drug Delivery,” *Biomaterials* 328 (2026): 123867, https://doi.org/10.1016/j.biomaterials.2025.123867.

64. R. J. M. Nolte, J. F. van der Pol, E. Neeleman, et al., “Liquid-Crystalline Phthalocyanines Revisited,” *Liquid Crystals* 33 (2006): 1373–1387.

65. Z. Huang, Y. Huang, W. Wang, et al., “Relationship Between Particle Size and Lung Retention Time of Intact Solid Lipid Nanoparticle Suspensions After Pulmonary Delivery,” *Journal of Controlled Release* 325 (2020): 206–222, https://doi.org/10.1016/j.jconrel.2020.06.004.

66. D. A. Cobb, N. Smith, S. Deodhar, et al., “Transformation of Tenofovir Into Stable Protide Nanocrystals With Long-acting Pharmacokinetic Profiles,” *Nature Communications* 12 (2021): 5458, https://doi.org/10.1038/s41467-021-25690-5.

67. M. Izci, C. Maksoudian, B. B. Manshian, and S. J. Soenen, “The Use of Alternative Strategies for Enhanced Nanoparticle Delivery to Solid Tumors,” *Chemical Reviews* 121 (2021): 1746–1803, https://doi.org/10.1021/acs.chemrev.0c00779.

68. A. Duro-Castano, V. J. Nebot, A. Niño-Pariente, et al., “Capturing “Extraordinary” Soft-Assembled Charge-Like Polypeptides as a Strategy for Nanocarrier Design,” *Advanced Materials* 29 (2017): 1702888, https://doi.org/10.1002/adma.201702888.

69. Y. Cao, J. Long, H. Sun, et al., “Dendritic Cell-Mimicking Nanoparticles Promote mRNA Delivery to Lymphoid Organs,” *Advanced Science* 10 (2023): 2302423, https://doi.org/10.1002/advs.202302423.

70. L. I. Moura, A. Malfanti, A. I. Matos, et al., “Off-The-Shelf Multivalent Nanoconjugate Cancer Vaccine Rescues Host Immune Response Against Melanoma,” *Advanced Materials* 37 (2025): 2417348, https://doi.org/10.1002/adma.202417348.

71. S. Thakur, V. Kumar, R. Das, V. Sharma, and D. K. Mehta, “Biomarkers of Hepatic Toxicity: An Overview,” *Current Therapeutic Research* 100 (2024): 100737, https://doi.org/10.1016/j.curtheres.2024.100737.

Supporting Information

Additional supporting information can be found online in the Supporting Information section.

Supporting File 1: adfm75799-sup-0001-SuppMat.pdf.

Supporting File 2: adfm75799-sup-0002-DataFile.xlsx.